



ISTITUTO NAZIONALE DI RICERCA METROLOGICA Repository Istituzionale

Refractive index gas thermometry between 13.8 K and 161.4 K

Original

Refractive index gas thermometry between 13.8 K and 161.4 K / Madonna Ripa, D; Imbraguglio, D; Gaiser, C; Steur, P P M; Giraudi, D; Fogliati, M; Bertinetti, M; Lopardo, G; Dematteis, R; Gavioso, R M. - In: METROLOGIA. - ISSN 0026-1394. - 58:2(2021), p. 025008. [10.1088/1681-7575/abe249]

Availability:

This version is available at: 11696/73210 since: 2022-02-18T14:54:23Z

Publisher:

IOP Publishing Ltd

Published

DOI:10.1088/1681-7575/abe249

Terms of use:

This article is made available under terms and conditions as specified in the corresponding bibliographic description in the repository

Publisher copyright

(Article begins on next page)



PAPER • OPEN ACCESS

Refractive index gas thermometry between 13.8 K and 161.4 K

To cite this article: D Madonna Ripa *et al* 2021 *Metrologia* **58** 025008

View the [article online](#) for updates and enhancements.

Refractive index gas thermometry between 13.8 K and 161.4 K

D Madonna Ripa¹ , D Imbraguglio¹ , C Gaiser² , P P M Steur¹ ,
D Giraudi¹, M Fogliati¹, M Bertinetti¹, G Lopardo¹ , R Dematteis¹ and
R M Gavioso^{1,*} 

¹ Istituto Nazionale di Ricerca Metrologica, Strada delle Cacce 91, 10135 Torino, Italy

² Physikalisch-Technische Bundesanstalt (PTB), Abbestrasse 2-12, 10587 Berlin, Germany

E-mail: r.gavioso@inrim.it

Received 6 November 2020, revised 8 January 2021

Accepted for publication 2 February 2021


Published 8 March 2021



Abstract

We have measured the refractive index of helium using a quasi-spherical copper microwave resonator at five different temperatures in the interval between the triple point of hydrogen at 13.8 K and the triple point of xenon at 161.4 K for pressures up to 380 kPa. From these results and additional measurements of the refractive index of neon near 54.4 K, 83.8 K and 161.4 K we determine the differences $(T - T_{90})$ between the thermodynamic temperature T and its approximation T_{90} by the International Temperature Scale of 1990 (ITS-90). We have estimated the isothermal compressibility of copper and the effective compressibility of our microwave resonator by different methods including resonant ultrasound spectroscopy (RUS) and microwave measurements with helium at 273.16 K. We compare the results of these compressibility estimates and discuss the associated uncertainty. From the refractive index measurements, we estimate the second density virial coefficient of helium and neon which are found in good agreement with the *ab initio* calculations of the same properties.

Keywords: refractive index gas thermometry, thermodynamic temperature, ITS-90, microwave resonator,

 Supplementary material for this article is available [online](#)

(Some figures may appear in colour only in the online journal)

1. Introduction

As a contribution to the ongoing effort to improve the consensus estimate of the differences $(T - T_{90})$ [1] we present some new determinations obtained by using the primary method denominated refractive index gas thermometry (RIGT) whose basic principle and procedures have been recently reviewed by Rourke *et al* [2]. These estimates, which span the temperature interval comprised between the triple point of hydrogen near 13.8 K and the triple point of xenon near 161.4 K, were

obtained using gaseous helium and neon as thermometric substances. Our results are found in good agreement with other recent determinations [3–10] of $(T - T_{90})$ obtained with several different primary thermometry methods in an overlapping temperature range.

1.1. Working equations and analytical methods

Our experimental determination of the refractive index $n(p, T)$ of a gas as a function of pressure p and thermodynamic temperature T relies on the possibility to measure the microwave resonance frequencies of a triaxial ellipsoidal copper cavity whose salient design and constructive features are described in section 2.1. With this instrument, $n(p, T)$ equals the ratio between the value of a resonance frequency of the evacuated cavity $f_m(0, T)$ and that of the same resonance $f_m(p, T)$ when

* Author to whom any correspondence should be addressed.



Original content from this work may be used under the terms of the [Creative Commons Attribution 4.0 licence](#). Any further distribution of this work must maintain attribution to the author(s) and the title of the work, journal citation and DOI.

the cavity is filled with gas at pressure p

$$n(p, T) = \frac{\langle f_m(0, T) \rangle}{\langle f_m(p, T) \rangle} \frac{1}{(1 - \kappa_{\text{eff}} p)}, \quad (1)$$

where the subscript m summarizes the mode type and order, the $\langle \dots \rangle$ brackets indicate averaging of the individual components of the resonances, which are at least triply degenerate for a quasi-spherical ellipsoidal cavity [11], and the corrective term defined by the *effective* compressibility κ_{eff} accounts for the change of the internal dimension of the cavity in response to a change of pressure. For most accurate work, this correction cannot be neglected and an independent estimate of κ_{eff} is needed. Such estimate is expected, and usually found [5], in close agreement with $\kappa_T/3$, where κ_T is the isothermal (volumetric) compressibility κ_T of the material comprising the resonator. In section 4 we discuss the result of our determination of κ_{eff} from auxiliary measurement of the refractive index of He at 273.16 K and a comparison with the determination of $\kappa_T/3$ by means of resonant ultrasound spectroscopy (RUS).

For the analysis of the experimental refractive index data, $n(p, T)$ is most conveniently expressed in the form of a power series of the pressure

$$n^2 = 1 + A_n p + B_n p^2 + C_n p^3 + \dots \quad (2)$$

with temperature-dependent coefficients given by combinations of the electromagnetic and thermodynamic properties of the gas:

$$A_n = \frac{3}{RT} (A_\varepsilon + A_\mu); \quad (3)$$

$$B_n = \frac{3A_\varepsilon}{R^2 T^2} (A_\varepsilon + b_\varepsilon - B_\rho); \quad (4)$$

$$C_n = \frac{3A_\varepsilon}{R^3 T^3} [A_\varepsilon^2 + c_\varepsilon - C_\rho + 2(b_\varepsilon - B_\rho)(A_\varepsilon - B_\rho)], \quad (5)$$

where R is the molar gas constant, A_ε and A_μ are the molar electric and magnetic polarizability at zero density and zero frequency, b_ε and B_ρ are the second dielectric and second density virial coefficients, and c_ε and C_ρ are the third dielectric and third density virial coefficients.

In this work, we determine T from our microwave data using different analytical methods discussed in detail in section 5.

In the first of these, dubbed *direct evaluation* in [2], T is the unknown in the implicit equation resulting from the combination of equations (1)–(5). This equation can be solved numerically at each thermodynamic state (p, T) if the properties of the gas are known from accurate *ab initio* theoretical calculations, using the measured value of p in the laboratory and an independent estimate of κ_{eff} .

Alternatively, from the entire collection of microwave data recorded at several different pressures along an isotherm, a single determination of T can be obtained by the procedure referred to in [2] as *ideal gas extrapolation*, i.e. by the fitted estimate of the linear pressure term h_1 in the combined

expansion of equations (1) and (3)

$$\left[\frac{f_m(0, T)}{f_m(p, T)} \right]^2 = 1 + h_1 p + h_2 p^2 + h_3 p^3 + \dots, \quad (6)$$

requiring the knowledge of the molar polarizabilities A_ε and A_μ and the compressibility κ_{eff}

$$T = \frac{3(A_\varepsilon + A_\mu)}{R(h_1 + 2\kappa_{\text{eff}})}. \quad (7)$$

We remark that the non-linear coefficients h_2, h_3, \dots in equation (6) may be themselves determined by fitting with a polynomial of suitable order, or alternatively constrained in a linear fit if the combinations of density- and refractive index virial coefficients which define them are independently known from theory. The latter choice, dubbed *hybrid analysis* in [2], may be more metrologically and statistically convenient if the theoretical estimate of h_2 is sufficiently accurate, which is in fact the case for He.

Finally, if the refractive index is measured at the same temperature and pressure for two different gases, like for the He and Ne data recorded near 54 K, 83 K and 161 K in this work, a determination of T is possible (*two gases method*) which does not require an independent estimate of the compressibility. With this procedure, the squared ratios of the microwave frequencies of the two gases are fitted by a polynomial expansion of the pressure

$$\left[\frac{f_{\text{He}}(p, T)}{f_{\text{Ne}}(p, T)} \right]^2 = 1 + \Omega_1 p + \Omega_2 p^2 + \Omega_3 p^3 + \dots, \quad (8)$$

and the thermodynamic temperature T is obtained by a combination of the fitted linear term in equation (8) and the polarizabilities of the two gases:

$$T = \frac{3(A_\varepsilon^{\text{Ne}} + A_\mu^{\text{Ne}} - A_\varepsilon^{\text{He}} - A_\mu^{\text{He}})}{R\Omega_1}, \quad (9)$$

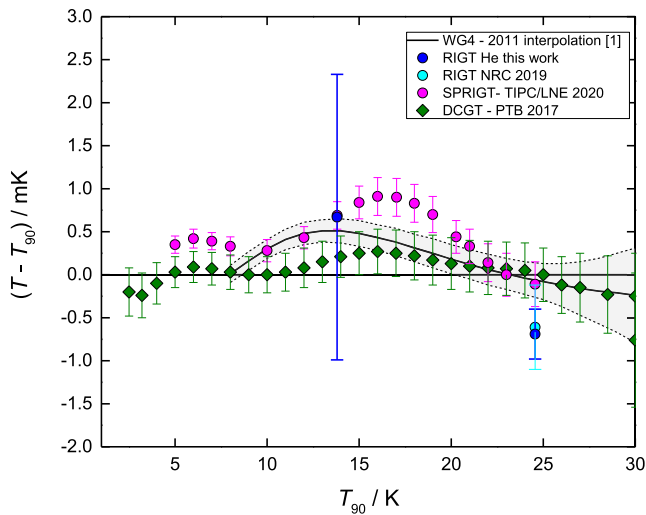
where, as in the isotherm method, the non-linear terms $\Omega_2, \Omega_3, \dots$ may be fitted using a polynomial or constrained in a linear fit.

1.2. Summary of $(T - T_{90})$ determinations

In section 5 we discuss and compare the different determinations of T which result from the alternative application of three analytical methods illustrated in the preceding section and their corresponding uncertainties. Anticipating the most relevant outcomes of this discussion, we remark that for the temperatures investigated in this work, the alternative application of the direct (p, T) single-state evaluation, the ideal gas extrapolation, and the hybrid method of analysis, all provided remarkably consistent $(T - T_{90})$ determinations. The results obtained by the hybrid analysis were the most accurate and are listed below in table 1, where the reported standard uncertainties are the quadrature sum of the contributions $u(T)$ of the microwave thermodynamic temperature determinations, listed in table 8 and table 9 and discussed in section 5, and the contributions $u(T_{90})$, listed in table 5 and discussed in section 3.

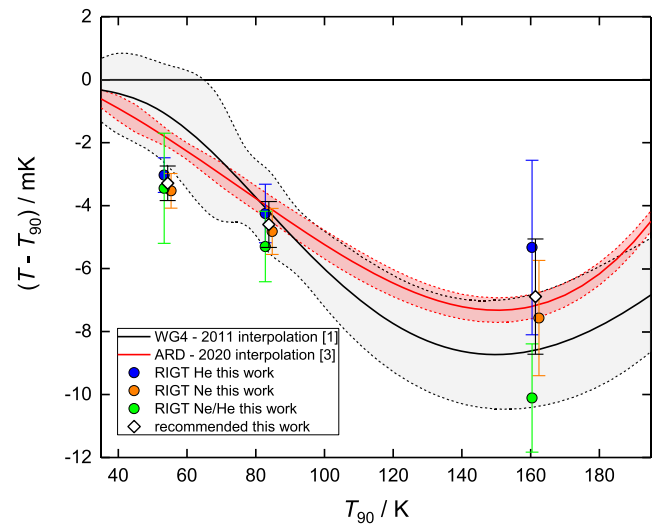
Table 1. Recommended $(T - T_{90})$ differences based on results obtained using two thermometric gases.

T_{90}/K	He	Ne	Recommended
		$(T - T_{90}) \text{ (mK)}$	
13.8033	0.67 ± 1.66		0.67 ± 1.66
24.5561	-0.69 ± 0.29		-0.69 ± 0.29
54.3584	-3.03 ± 0.55	-3.53 ± 0.55	-3.29 ± 0.55
83.8058	-4.25 ± 0.93	-4.82 ± 0.73	-4.60 ± 0.73
161.4060	-5.33 ± 2.77	-7.57 ± 1.83	-6.89 ± 1.83


Figure 1. Comparison of the $(T - T_{90})$ determinations obtained in this work with the interpolating equation developed by Fischer *et al* [1]—black line and grey shaded area—and other recent results obtained by RIGT [4, 5], DCGT [9] and SPRIGT [6] in the temperature range below 30 K.

Additionally, where $(T - T_{90})$ results were available for both He and Ne, the single recommended result in the rightmost column of table 1 is their weighted mean and, because the results are highly correlated, the uncertainty is conservatively assumed to be the lowest uncertainty of the individual measurements.

For the temperature range spanning below 30 K, figure 1 displays the results obtained in this work from the analysis of He data, which are compared and found to be mostly consistent with other recent $(T - T_{90})$ determinations, including those obtained by RIGT at the National Research Council of Canada (NRC) [4, 5], by single pressure RIGT (SPRIGT) at the Technical Institute of Physics and Chemistry of the Chinese Academy of Science (TIPC-CAS) in collaboration with the Laboratoire National de Métrologie et d'Essais (LNE) [6], and by dielectric constant gas thermometry (DCGT) at the Physikalisch-Technische Bundesanstalt (PTB) [3, 9]. Unfortunately, the large uncertainty affecting our result at 13.8 K, which is primarily ascribable to the instability of the standard platinum thermometers between two successive calibrations (see section 3.1), reduces the relevance of the comparison and its utility for a future revision of $(T - T_{90})$. Otherwise, the


Figure 2. Comparison of the $(T - T_{90})$ determinations obtained in this work with two interpolating equations, respectively based on primary thermometry results obtained until 2011 or after that date. The former, developed by Fischer *et al* [1] is plotted as a black line with grey shaded area displaying the uncertainty. The latter, developed by Gaiser *et al* [3] is plotted as a red line with the light red shaded area displaying the uncertainty. Plotted symbols display the $(T - T_{90})$ recommended differences obtained in this work, the individual results obtained using He or Ne, and the additional results obtained by a combined analysis of He/Ne microwave frequency ratios. Plotted symbols for different gases are slightly offset on the temperature axis to ease their visual comparison.

result at 25.4 K is found to in remarkable agreement with the RIGT determination of NRC and with the acoustic gas thermometry (AGT) result reported in 2006 by the National Institute of Standards and Technology (NIST) and LNE [12], but is slightly inconsistent with the interpolating equation of primary thermometry results before 2011 and with the SPRIGT results of TIPC-CAS and the DCGT results of PTB.

Figure 2 displays our recommended $(T - T_{90})$ results, together with those obtained from the individual analysis of He and Ne data, as well as their combination by the two-gases analysis with equations (8) and (9), for the temperature range between 30 K and 200 K where, in addition to the 2011 interpolation, a very precise interpolation of post-2011 results has been recently evaluated [3]. The latter is based on the RIGT results of NRC [4, 5], the DCGT results of PTB [3, 9], and the accurate AGT results of the National Physical Laboratory [7]. Figure 2 shows that, at all temperatures, the RIGT results obtained in this work, using He or Ne as the thermometric gas, were found to be mutually consistent.

Also shown in figure 2 are the $(T - T_{90})$ differences obtained by the analysis of combined He/Ne microwave frequency ratios, as discussed in section 5.4. With the exception of the isotherm at 161.4 K, the results obtained with two gases have a significantly larger uncertainty compared to those based on single gases and were not included in the combined evaluation of the recommended list in table 1.

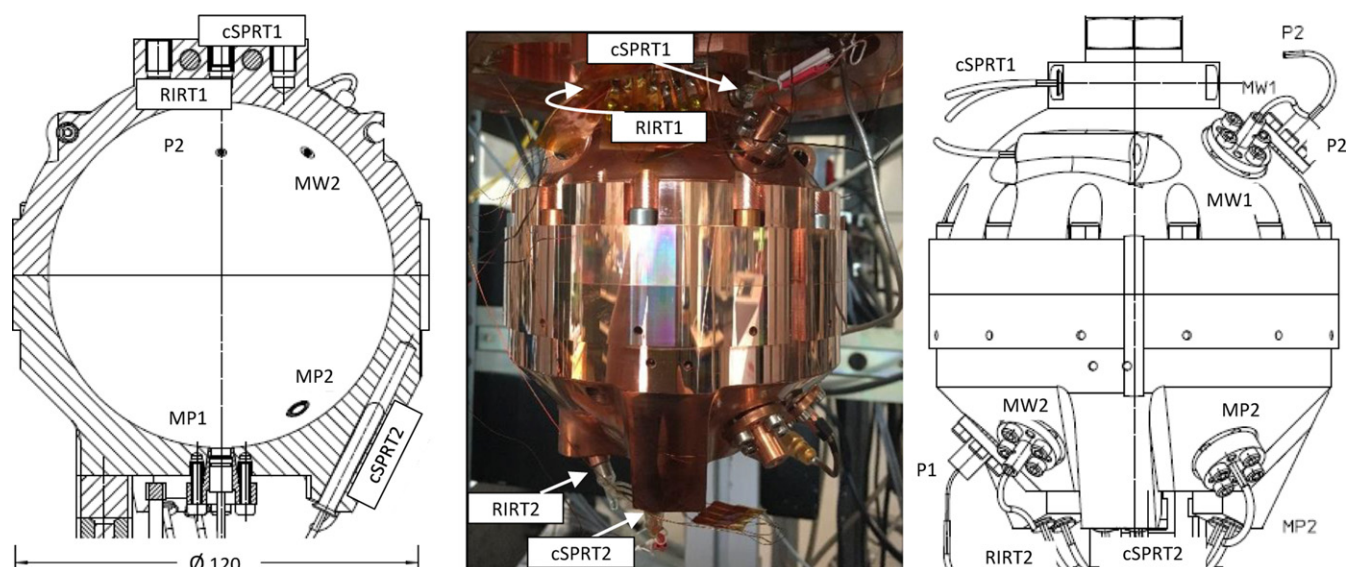


Figure 3. Cross section and sketches of the microwave cavity showing location of gas inlet-outlet ports (P1, 2), microwave antennas (MW1, 2), microphones (MP1, 2—not used in this work) and capsule type platinum and rhodium–iron resistance thermometers (cSPRT1, 2; RIRT1, 2).

2. Experimental apparatus

2.1. Microwave resonator

The microwave resonator used in this work is a hollow quasi-spherical cavity made in electrolytic tough pitch copper (Cu-ETP). It comprises two nominally identical hemispheres machined and diamond-turned in 2017 by Savimex sas^{3,4} under supervision and following the technical design provided by LNE-CNAM. Two nearly identical copies of the cavity were fabricated from the same batch of copper. One of these copies was recently used at the Technical Institute of Physics and Chemistry of the Chinese Academy of Science (TIPC-CAS) to achieve accurate determinations of the thermodynamic temperature between 5 K and 24.5 K [6]. The second copy is in use at NRC to develop a primary acoustic gas thermometer. Upon its assembly at INRiM, the internal shape of the cavity approximates a triaxial ellipsoid with semi-axes: $a_x = 50.050$ mm; $a_y = a_x (1 + \varepsilon_1) = 50.100$ mm; $a_z = a_x (1 + \varepsilon_2) = 50.075$ mm at ambient temperature, where ε_1 and ε_2 quantify the designed deviations from sphericity. Such slight deformation facilitates a precise determination of the resonance frequency by lifting the intrinsic degeneracy of the microwave modes of a perfect sphere, a successful strategy well documented by the previous utilization of this type of cavities for accurate work in primary thermometry and pressure metrology [11–14]. Up to six ports bored through the resonator wall and matching copper adapters allow fixture of microwave cables terminated by antennas, acoustic transducers (not used in this work) or gas ducts. Unused ports are closed

by blank plugs whose front surface reproduces the internal surface shape and finishing of the cavity. Eight additional ports, distributed at different locations along the external profile of the cavity, are available for the location of capsule-type thermometers. Figure 3 shows a detail of a typical experimental configuration.

2.2. Cooling and temperature control system

For temperature control of the microwave cavity in the range between 9 K and ambient temperature, a cryostat comprised by three main vacuum-tight stages was realized and assembled, as shown in figure 4. The cryostat design and principles were inspired by those recently used in a single-pressure RIGT apparatus [15]. It employs a pulse-tube cryocooler (PTC), Sumitomo model SRP-082B2S-F70H, delivering a cooling power of 0.9 W at 4.2 K. The innermost stage of the cryostat is a cylindrical copper vessel with an internal diameter (i.d.) of 200 mm, referred to as *experimental vessel*, which contains and supports the microwave cavity. The top end of the cavity is loosely attached to the flange of the experimental vessel by a bolted copper post providing a weak thermal link, while the bottom end of the cavity remains suspended without direct contact to the vessel. Across the main flange of the experimental vessel, a number of coaxial and single pin feedthroughs are welded on three stainless steel (ss) smaller flanges to allow transmission of microwave signals and to provide electrical contact to the terminals of the thermometers. An additional custom flanged copper block is internally bored by a 4 mm hole to allow for evacuation and filling of the experimental vessel with the test gas.

Around the experimental vessel, a larger (i.d. 250 mm) vacuum-tight cylindrical copper vessel equipped with the same number and type of hydraulic- and electrical-feedthroughs detailed above, serves as a *thermal switch* stage, which favors or minimizes heat transmission between the PTC and the

³ Identification of commercial equipment and materials in this paper does not imply recommendation or endorsement by INRiM, LNE-CNAM or PTB nor does it imply that the equipment and materials identified are necessarily the best available for the purpose.

⁴ SAVIMEX sas, 1 Avenue Louison Bobet, 06130 Grasse (F).

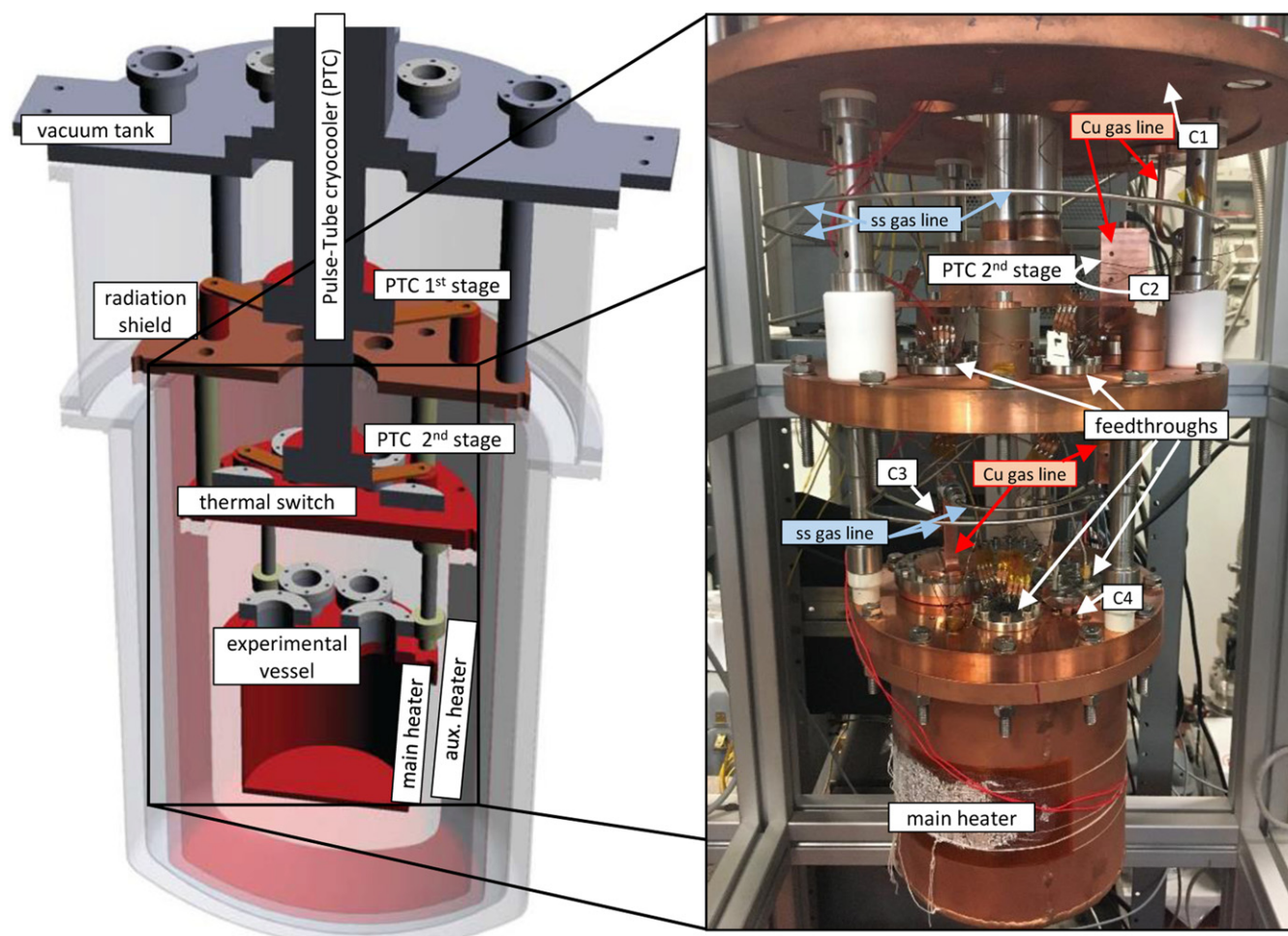


Figure 4. (Left) 3D sketch of the different parts and stages comprising the cryostat used in this work. (Right) picture showing details of the experimental vessel and the thermal switch and radiation shield top flanges. Text labels and arrows point at the position of four Cernox[®] temperature sensors with (C1–C4) used to evaluate the temperature distribution along the gas line and PID control the temperature of the experiment. Isothermal vertical copper sections and isobaric horizontal spiraling ss sections of the gas line are indicated by red and light blue labels and arrows respectively.

experimental vessel. The thermal switch is filled with gas, at a pressure in the order of 100 Pa, to speed up large desired changes of the temperature experimental set-point, while it is evacuated to enhance thermal stability of the experimental vessel during normal operation, i.e. for microwave data recording. Thermal contact between the 2nd stage of the PTC and the outer flange of the thermal switch is provided by a set of cylindrical copper posts and rectangular plates to attain vertical and radial clearance for feedthroughs, connectors and thermal anchoring of cables and tubing. The next outer surrounding stage is a cylindrical copper enclosure (i.d. 320 mm) which serves as a *radiation shield* to minimize heat losses between the 1st stage of the PTC and the thermal switch on one side, and the ambient temperature surrounding tank on the other side. An effective thermal link between the radiation shield and the PTC is provided by a set of copper posts and plates similar to those installed on the thermal switch.

Finally, all the elements and parts described above are contained by a ss vacuum-tight cylindrical tank (i.d. 500 mm, 500 mm deep) fit with several welded trunk ConFlat[®] flanges

used to feedthrough experimental signals, gas inlet and outlet flows and to connect electrical heaters and auxiliary temperature sensors distributed along the cryostat. In addition to the solid shield described above, Mylar foil was used to reduce radiation heat losses between the different stages comprising the cryostat. The main and secondary flanges on both the experimental and thermal switch vessels were sealed for vacuum and pressure-tightness using indium wire.

The complete assembled system was tested for vacuum tightness, using a He leak detector, and cooling performance in the course of 2017 reaching a minimum temperature on the 2nd stage of the PTC of 3.2 K. In January 2018, the microwave resonator was mounted within the experimental vessel. The additional heat losses introduced by cables and gas tubes limited the minimum operating temperature of the apparatus to about 9 K.

In the range between 13 K and 161 K, the working temperature of the experimental vessel was set by supplying electrical power from a 200 W programmable DC source, Keysight E3634A, to a 85 Ω Kapton thermofoil heater in contact with the external cylindrical body of the vessel. Fine

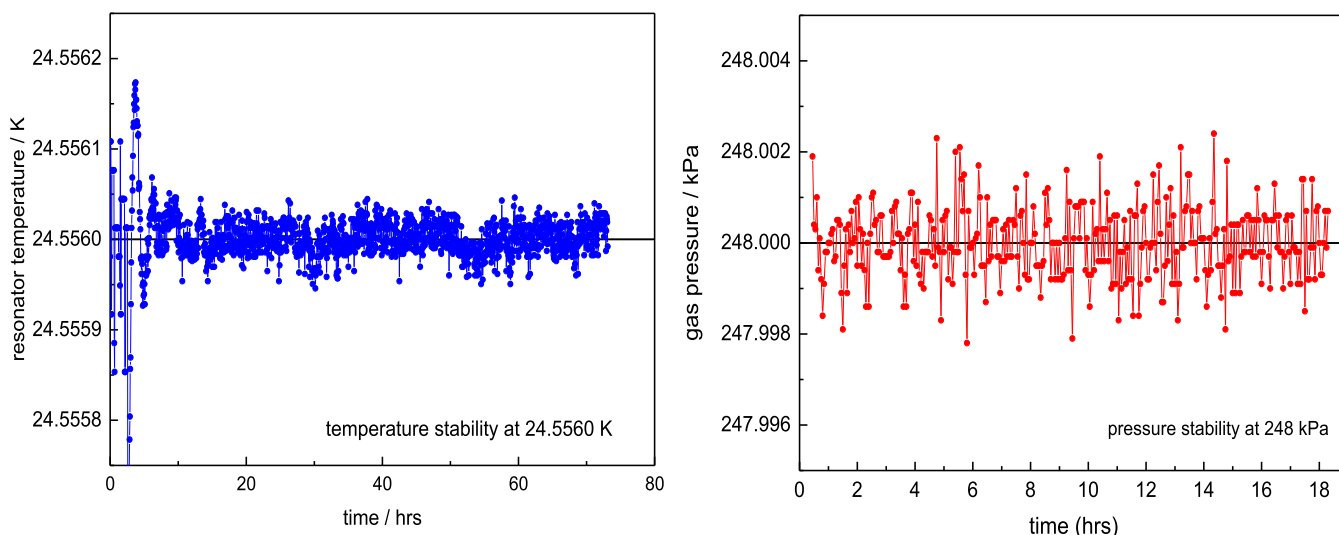


Figure 5. (Left plot) Temperature stability, measured by a platinum resistance thermometer in contact with the microwave cavity when filled with He at 250 kPa and regulated by PID control near 25 K. (Right plot) pressure stability achieved by PID control of the pressure in the same experimental conditions.

regulation of the heating power was driven by a proportional–integral–derivative (PID) algorithm. Figure 5 shows the long-term stability, better than 0.05 mK, achieved by the PID control of the resonator temperature when it is maintained near 25 K with the experimental vessel filled at 250 kPa and the thermal switch evacuated. An auxiliary 470 Ω thermofoil heater in contact with the thermal switch vessel provided the additional power needed to thermostat the experiment near 273.16 K for the determination of κ_{eff} discussed in section 4.2. A set of four calibrated Cernox[®] thin film resistance temperature sensors was deployed in the cryostat; one of those, contacting the top flange of the experimental vessel was used to PID control the temperature of the experiment; the remainders, placed along the line driving gas between the ambient and the resonator, were used to estimate the temperature differences needed to evaluate the hydrostatic head correction of the gas pressure discussed in the following section. The resistance of the Cernox[®] sensors was measured using a digital Keithley 2002 multimeter, whose specifications amply suit the need for an accurate evaluation of the head correction.

2.3. Pressure measurement and control—gas purity

The gas handling system used in this work (figure 6) is comprised by two main parts: a manifold assembled in the laboratory environment; a gas line, resulting by the junction of several copper and ss sections, embedded in the cryostat, which connects the external manifold to the internal volume of the experimental vessel.

In operation, the pressure in the manifold is measured using two quartz sensors with full-scale ranges of 207 kPa (Paroscientific 745-30A) and 690 kPa (Paroscientific 745-100A) respectively. In reason of its lower range, the former transducer enhances precision and repeatability; however, it must be manually isolated from the manifold when the experimental pressure is set above 200 kPa. In order to enhance the precision and stability of the experimental pressure (see figure 5),

which would otherwise be affected by fluctuations of the ambient temperature of the laboratory, gas was continuously flown through the manifold at the rate of 10 sccm, set constant by a mass-flow controller, while the pressure reading from the quartz transducer regulated the variable opening of a solenoid electrically actuated valve, MKS 0248AC-00500SV, based on a PID algorithm. The gas line within the cryostat is set on a dead-end branch of the manifold and the exchange of gas with the rest of the manifold ineffectively takes place only by thermal diffusion. The gas line itself (figure 6) is composed by the alternate junction of three horizontal isobaric 1/8-inch ss segments, 1 m to 2 m long, to custom-machined flanged isothermal copper posts whose combination vertically develops to cover the total height difference between the resonator and the top of the vacuum tank. These posts are internally bored by 4 mm diameter ducts and heat-sunk to the experimental vessel and the two cooling stages of the cryostat. This system simplifies the calculation of the pressure correction accounting for the aerostatic weight of the gas column, as first suggested by Astrov *et al* [16] and recently discussed by Pan *et al* [17]. In our working conditions the pressure correction spans between a minimum of 5.1 Pa when He fills the apparatus at 80 kPa, 161 K, which is relatively equivalent to 63 ppm, and a maximum of 50.4 Pa at 280 kPa, 54.3 K or equivalently 180 ppm when Ne fills the apparatus.

After completing the recording of microwave data at each pressure point along an isotherm, the gas line of the cryostat was manually isolated and the quartz transducers calibrated by comparison with the more accurate pressure standard provided by a pressure balance (DHI/Fluke PG7601). The balance is equipped with an automatic mass handling system and operated in absolute mode, with the bell jar evacuated to avoid the need and the additional uncertainty of a buoyancy correction. The value of the effective area $A_{\text{eff},0} = (1.961\,160 \pm 0.000\,011) \times 10^{-4} \text{ m}^2$ of the piston-cylinder assembly (PG1606), which is equivalent to a relative standard uncertainty of

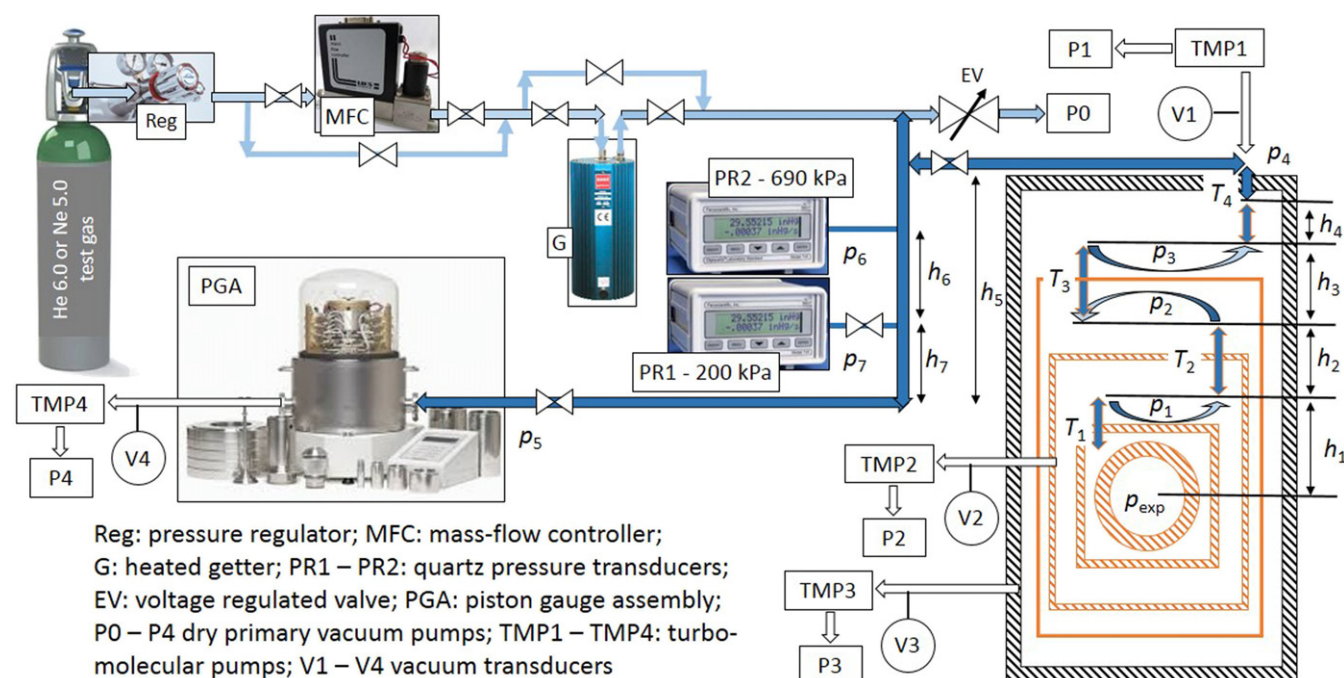


Figure 6. Diagram of gas manifold used to regulate and measure pressure in the RIGT apparatus. Light-blue color delimits the portion of the manifold kept under continuous flow to precisely control the pressure. Temperature measurements T_1 to T_4 , at different locations along the cryostat, were used to calculate a hydrostatic pressure correction based on the extension, h_1 to h_4 , of vertical isothermal copper tube sections connected by horizontal isobaric, p_1 to p_4 , ss tube sections.

5.5 ppm, and the values of the mass set installed on the balance were calibrated and communicated by the manufacturer. The value of the local gravity at INRiM campus was assumed to be $(9.805\,340 \pm 0.000\,002) \text{ m s}^{-2}$ from a previous reported assessment [18]. All these assumptions lead to an overall relative uncertainty of the pressures reproduced by the piston gauge ranging between a maximum of 18 ppm at 34 kPa and a minimum of 11 ppm at 1871.2 kPa.

Nominally 99.9999% (6.0) pure He and 99.999% (5.0) pure Ne, as specified by the manufacturers, were used in this work. Further reduction to low parts per billion (ppb) levels of the most common, chemically reactive, possible residual impurities, including O_2 , H_2O , CO , CO_2 , H_2 , CH_4 and N_2 was achieved by flowing through an SAES PS2 GC50 heated getter. In principle, contamination from trace amounts of inert gases different from that under test, which would not be removed by the getter, is possible. Unfortunately, dedicated mass-spectrometric analyses for the samples used in this work were not available. However, based on the results of these analyses for the same type of He and Ne sources used in this work [8, 9, 19], the additional uncertainty contribution of plausible amounts of trace contaminants to our determinations of T is well below the 1 ppm level and, as such, negligible in the present uncertainty context. The possible contamination of Ne from traces and virtual leaks of He remaining in the apparatus after the conclusion of measurements with this test gas causes more concern. The remarkable agreement of the RIGT results obtained with both He and Ne is indeed reassuring with regard to this issue.

2.4. Microwave measurements and perturbation model

The resonance frequencies appearing in equation (1) were experimentally estimated by recording and fitting microwave data for 6 different electromagnetic modes, namely TM11, TM12, TM13, TE12, TE13, TE14. With a few exceptions discussed below, these measurements employed ordinary instrumentation, procedures and statistical tools as previously used at INRiM for precise primary gas thermometry with spherical resonators [19, 20]. Basically, in this work these require the coaxial cable connection of the two ports of a vector network analyzer (VNA), Agilent E5071C, to a couple of ‘L’ shaped antennas slightly protruding (by a few millimeters) within the microwave cavity. The cables (0.085’ o.d.) are routed across the hermetic seals of the vacuum tank, the thermal switch and the experimental vessel by SMA feedthroughs welded to ss flanges at each stage. In order to enhance the S/N ratio of the microwave signal, otherwise depleted by the absorption loss due to the relevant total length of the cables, a microwave amplifier (Mini circuits mod ZX60-14012L) with a gain of 12 dB was inserted close to the receiving port of the VNA, as first suggested in [21]. With this arrangement, coupling of our antennas to the electromagnetic field within the cavity was found to be much more effective for TM modes than for TE modes, with a resulting relative fitting precision varying between a few parts in 10^{10} for TM modes to several parts in 10^8 for TE modes. Such a relevant difference in precision made the TE modes much less weightful for the determination of the refractive index and their data were not used for the

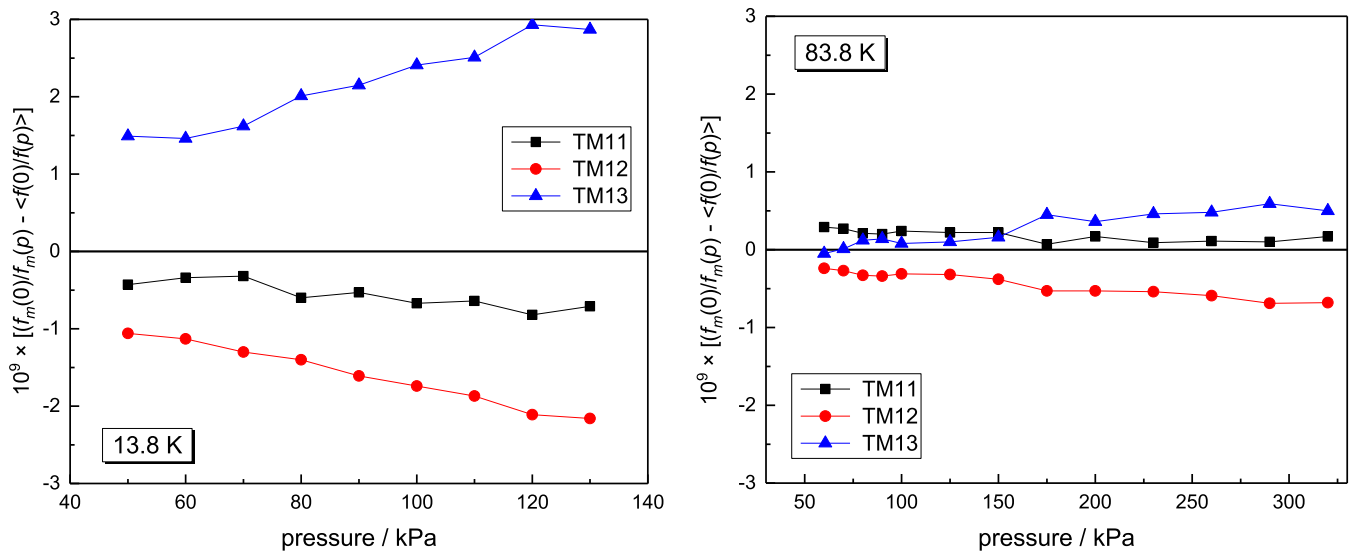


Figure 7. Relative differences of frequency ratios calculated from three TM modes from their mean upon correction using equation (10) at 13.8 K (left plot) and 83.8 K (right plot).

determination of the thermodynamic temperatures discussed in section 5. The figures of merit reported above were obtained by setting the output power of the VNA to +10 dBm or, equivalently, 10 mW. At 25 K in vacuum, a reduction of the output power of the VNA by a factor of three, from +10 dBm to +5 dBm (eq. to 3.2 mW), decreased the temperature of the cavity by approximately 4 mK. However, this change had no appreciable effect (relatively less than 1 part in 10^9) on the mode frequencies when these were corrected to account for the decreased dimensions of the cavity using a coarse estimate of the thermal expansion coefficient of copper. The same test was later repeated at 25 K, with the cavity filled with He at a pressure of 80 kPa, showing that the thermal gradient estimated by the readings of two capsule-type standard platinum resistance thermometers (cSPRTs) remained unaltered, within 200 μ K, by the reduction in microwave power.

In principle, the accurate determination of the refractive index n from the vacuum/pressure frequency ratios $\langle f_m(0, T) \rangle / \langle f_m(p, T) \rangle$ in equation (1) requires that the frequencies would be preliminarily corrected to account for perturbing physical effects. Of these, that caused by the finite penetration depth of the electric field within the cavity metal wall, briefly referred to as skin effect, is the mostly relevant. In this work, the correction is accounted for by the addition to the average fitted experimental resonance frequency $\langle f_m^{\text{exp}}(p, T) \rangle$ of each mode m of a corresponding calculated halfwidth $g_m(p, T)$ based on the estimate of the electrical resistivity of the internal surface of the copper cavity ρ_{Cu} determined from the average fitted halfwidth of mode TM11

$$f_m(p, T) = \langle f_m^{\text{exp}}(p, T) \rangle + g_m(p, T). \quad (10)$$

The particular choice of mode TM11 was driven by the observation that among the set of investigated modes, at all temperatures, it provides the lowest value of ρ_{Cu} . This was found to vary between 1.24 n Ω m at 9 K and 16.4 n Ω m at 273 K with a resulting residual resistivity ratio RRR \sim 13.

These values of ρ_{Cu} do only slightly differ (by at most 7%) from those reported for oxygen-free high-conductivity (OFHC) copper, having a comparable RRR, in the same temperature range [22, 23]. The corresponding quality factor of the resonances varied between a minimum of 4.0×10^4 for mode TM11 at 161.4 K and 2.7×10^5 for mode TE14 at 13.8 K.

The simple correction model of equation (10) assumes that the resistive and reactive components of the microwave surface impedance of copper are equal, and does not account for the complications introduced by the anomalous skin effect taking place at low temperature and high frequency [24]. Evidence of these anomalies was revealed by the systematic frequency dependence of ρ_{Cu} estimated from various modes. For instance, at 13.8 K ρ_{Cu} estimated from $\langle g_{\text{TM11}} \rangle$ at 2.6 GHz is found relatively lower by 40% than ρ_{Cu} estimated from $\langle g_{\text{TE14}} \rangle$ at 13.4 GHz; the relative difference decreases with increasing temperature to 12% at 83 K and to less than 3% at 161 K. In spite of these anomalies, the relative dispersion of the ratios $f_m(0, T)/f_m(p, T)$ determined for different modes by the simple correction model of equation (10) is extremely small, at the level of ± 3 parts in 10^9 (ppb) for the more precise TM modes (see figure 7).

Also, the consequences of any alternative correction to account for skin effect perturbations from that represented by equation (10) would have minor consequences. In fact, as evidenced in figure 8, even without correction of the experimental frequencies, the resulting change in the estimated frequency ratios $f_m(0, T)/f_m(p, T)$ would be relatively less than 3 ppb in the worst case and thus irrelevant given the present uncertainty context. The same is true if the experimental halfwidths $\langle g_m^{\text{exp}}(p, T) \rangle$ of each mode are used in equation (10) instead of the $g_m(p, T)$ based on the resistivity estimate from mode TM11 only.

Models and experimental verifications are also available to account for the perturbing effect of waveguides and holes [25],

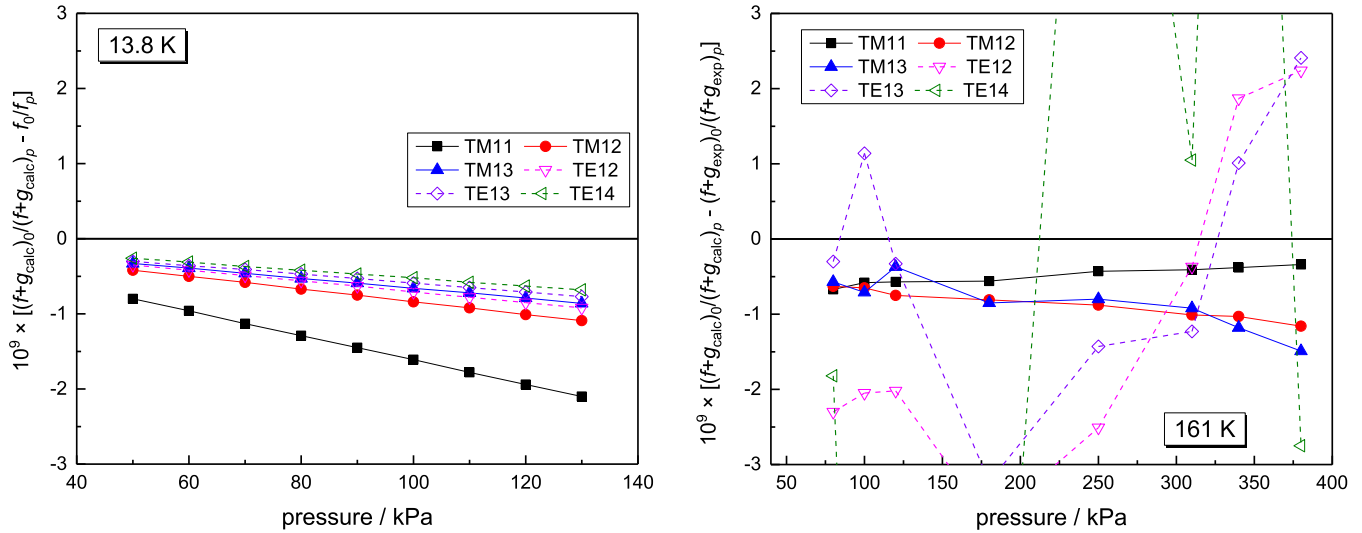


Figure 8. (Left) Relative differences between frequency ratios of TM and TE modes at 13.8 K corrected for skin effect using equation (10) or alternatively uncorrected. (Right) Relative differences between frequency ratios of TM and TE modes at 161 K corrected for skin effect using equation (10) or alternatively by using the experimentally fitted halfwidth of each mode.

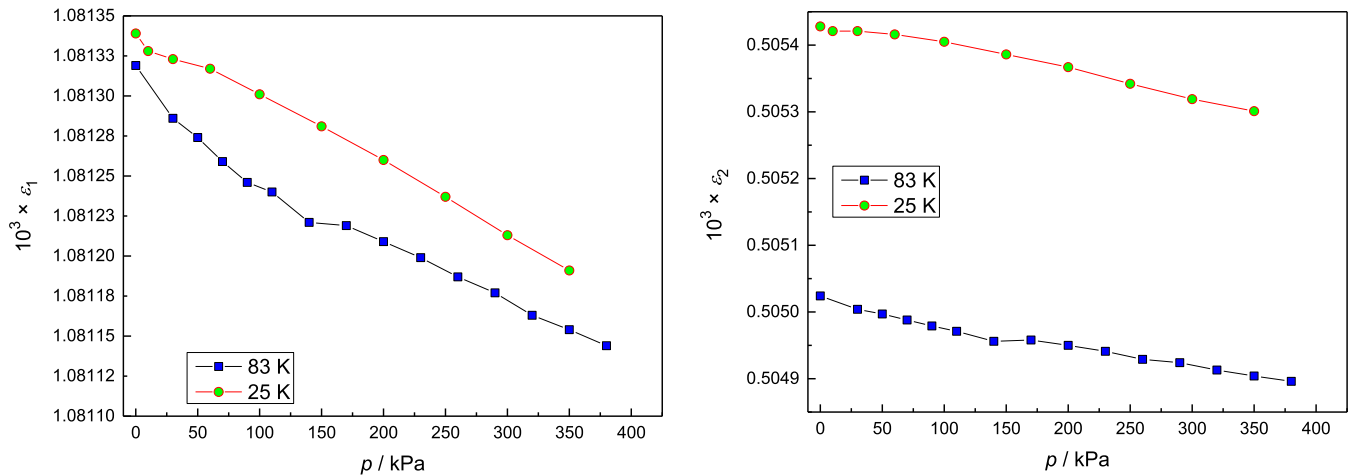


Figure 9. Geometrical shape factors ϵ_1 (left plot) and ϵ_2 (right plot) which define the deviation of the internal geometrical shape of the resonator from that of a perfect sphere. The small recorded variation of these parameters as a function of pressure up to 370 kPa for two test temperatures at 25 K and 83 K indicate that geometrical corrections for the microwave eigenfrequencies recorded in this work can be safely neglected in the simple correction model described by equation (10).

with predicted corrections which are considerably smaller than those due to the finite resistivity of the surface and do not depend on pressure. As such, they were not considered in this work due to their irrelevance for the evaluation of $f_m(0, T)/f_m(p, T)$. To check that this is also the case for the geometrical perturbations induced by possible changes of the resonator shape as a function of pressure, we examined the variation of the shape parameters ϵ_1 and ϵ_2 determined from the relative dispersion of the single components within each degenerate mode. In good agreement with the designed specifications for manufacturing we found $\epsilon_1 \sim 2\epsilon_2 \sim 1.08 \times 10^{-3}$. The pressure variations of these parameters, displayed in figure 9 for 25 K and 83 K and pressures up to 380 kPa, resulted less than 1.5×10^{-7} . The pressure variation of the corresponding geometrical corrections to the mode eigenfrequencies, which can be calculated using the perturbative model

elaborated by Mehl [26], are so small that the effect of their inclusion in the simple correction model described by equation (10) and their effect on the determination of the ratios $f_m(0, T)/f_m(p, T)$ would be irrelevant.

3. Determination of T_{90}

The International Temperature Scale of 1990 (ITS-90) [27] approximation T_{90} of the thermodynamic temperature of the gas was inferred from the resistance of two calibrated cSPRTs (Chino mod. R800-0) placed in thermal contact with the microwave cavity. The cSPRTs with serial numbers RS144-01 and RS158-04 were respectively located at the top and bottom end of the cavity (see figure 3). Two rhodium–iron resistance thermometers (RIRTs) were also calibrated and

Table 2. $R_{90}(T_{90})$ values resulting from the calibration of two cSPRTs in 2018 and 2020, before and after RIGT measurements, and variations of resistance $\Delta R_{20-18} = (R_{90,2020} - R_{90,2018})$ and of the corresponding temperatures ΔT_{20-18} . The uncertainty $u(T_{90})$ values is the combined standard uncertainty ($k = 1$) of a single fixed-point calibration of a single cSPRT [28]. The typical sensitivity factors dT/dR are those discussed in [33].

Triple point	T_{90} (K)	$u(T_{90})$ (mK)	dT/dR (K Ω^{-1})	RS144-01				RS158-04			
				$R_{90,2018}$ (Ω)	$R_{90,2020}$ (Ω)	ΔR_{20-18} (m Ω)	ΔT_{20-18} (mK)	$R_{90,2018}$ (Ω)	$R_{90,2020}$ (Ω)	ΔR_{20-18} (m Ω)	ΔT_{20-18} (mK)
e-H ₂	13.8033	0.10	166.2	0.037 9100	0.037 9478	0.038	6.30	0.028 6141	0.028 6336	0.019	3.24
Ne	24.5561	0.07	32.6	0.220 8451	0.220 8659	0.021	0.68	0.213 3557	0.213 3633	0.008	0.25
O ₂	54.3584	0.06	10.2	2.311 5515	2.311 5975	0.046	0.47	2.334 2272	2.334 2587	0.031	0.32
Ar	83.8058	0.05	9.2	5.428 9764	5.429 0109	0.034	0.32	5.496 4110	5.496 4435	0.032	0.30
Hg	234.3156	0.06	9.9	21.208 149	21.208 199	0.050	0.50	21.500 756	21.500 894	0.137	1.36
TPW	273.1600	0.03	10.0	25.122 533	25.122 709	0.176	1.76	25.470 982	25.471 223	0.241	2.41

Table 3. $W_{90}(T_{90})$ values resulting from the calibration of two cSPRTs in 2018 and 2020, before and after RIGT measurements, and variations of resistance ratio $\Delta W_{20-18} = (W_{90,2020} - W_{90,2018})$ and of the corresponding temperatures ΔT_{20-18} . The uncertainty $u(T_{90})$ values is the combined standard uncertainty ($k = 1$) of a single fixed-point calibration of a single cSPRT [28]. The typical sensitivity factors dT/dW (T_{90}) are those discussed in [33].

Triple point	T_{90} (K)	$u(T_{90})$ (mK)	dT/dW (K)	RS144-01				RS158-04			
				$W_{90,2018}$	$W_{90,2020}$	ΔW_{20-18}	ΔT_{20-18} (mK)	$W_{90,2018}$	$W_{90,2020}$	ΔW_{20-18}	ΔT_{20-18} (mK)
e-H ₂	13.8033	0.10	4155	0.001 5090	0.001 5105	0.000 0015	6.22	0.001 1234	0.001 1242	0.000 0008	3.13
Ne	24.5561	0.07	815	0.008 7907	0.008 7915	0.000 0008	0.62	0.008 3764	0.008 3766	0.000 0002	0.18
O ₂	54.3584	0.06	256.2	0.092 0111	0.092 0123	0.000 0012	0.30	0.091 6426	0.091 6430	0.000 0004	0.09
Ar	83.8058	0.05	230.3	0.216 0999	0.216 0997	-0.000 0001	-0.03	0.215 7911	0.215 7903	-0.000 0008	-0.18
Hg	234.3156	0.06	247.7	0.844 1883	0.844 1844	-0.000 0039	-0.97	0.844 1275	0.844 1249	-0.000 0026	-0.64

initially installed on the cavity, intended to provide a more precise temperature reference at 13.5 K. Unfortunately, a faulty electrical wiring of one RIRT prevented its use as scheduled, and the estimate of T_{90} was necessarily based on the readings of the two cSPRTs over the entire range of temperatures (13.5 K to 273.16 K) explored in this work.

3.1. Calibration of capsule-type thermometers

Both cSPRTs were calibrated in 2018 and in 2020, with slightly different procedures, before and after the RIGT measurements which took place in 2019 over the course of nearly one year. The reader is referred to [28] for a detailed account of the apparatus and the calibration procedures available at INRiM for the realization of ITS-90 between 13 K and 273 K. Both the 2018 and the 2020 calibration procedures involved the direct realization of the triple points of neon ($T_{90} = 24.5561$ K), oxygen ($T_{90} = 54.3584$ K) and argon ($T_{90} = 83.8058$ K) in an adiabatic cryostat with the calorimetric method [29], and the insertion of the cSPRTs into the standard cells for the realization of the triple points of mercury ($T_{90} = 234.3156$ K) and water ($T_{90} = 273.1600$ K) realized using the continuous heating method [30, 31]. In order to fit the capsule thermometers into the water and mercury standard sealed cells, which are conceived for the calibration of long-stem SPRTs, suitable custom adapters designed at INRiM were used. The adapters, comprised by two mountable sections of ss tube for a total length of approximately 600 mm, internally embed

miniature four-wire connectors and soldering terminals. The front tip of the adapters, to enhance thermal contact with the housed cSPRT, is a 45 mm long OFHC copper jacket. Upon assembly, the adapters are filled with air and are sealed by Viton O-rings to avoid infiltration from the liquid in the well of the fixed point cells. The triple point of equilibrium hydrogen ($T_{90} = 13.8033$ K) was directly realized only for the 2020 calibration, while in 2018 the cSPRTs were calibrated near 13.8 K by comparison with the wire scale maintained by a national standard reference (RIRT 232324). This alternative procedure was necessary in 2018 due to the limited operating range of the cryocooler serving direct realization of the cryogenic fixed points.

The calibration results are summarized in tables 2 and 3, which respectively list the thermometer resistances R_{90} , evaluated by the direct realization of each fixed point, and the corresponding $W_{90}(T_{90})$ values. We remark that all the R_{90} in table 2 were obtained from original calibration data upon applying the corrections needed to account for the isotopic content of the standard sealed cells, as established in the *Technical Annex for the ITS-90* of the *Mise en pratique* for the definition of the kelvin [32], and those due to the hydrostatic pressure within the fixed-point cell. Also, the tabulated R_{90} values were previously extrapolated to zero current and, where applicable, refer to a melted fraction $F = 1$.

With the exception of the measurements recorded near 161 K, all the other RIGT determinations of the thermodynamic temperature reported in this work are based on

Table 4. Budget of relevant uncertainty contributions to the determination of T_{90} .

T_{90} (K)	13.8033	24.5561	54.3584	83.8058	161.4060	54.3584	83.8058	161.4060
Thermometric gas			He				Ne	
Uncertainty source	Standard uncertainty $u(T_{90})$ (mK)							
Calibration uncertainty	0.78	0.07	0.06	0.05	0.23	0.06	0.05	0.23
Resistance measurements	0.08	0.06	0.04	0.02	0.01	0.04	0.02	0.01
Thermal gradient across resonator	0.44	0.08	0.10	0.22	0.57	0.06	0.14	0.19
Thermometers' drifts	1.38	0.13	0.11	0.09	0.08	0.11	0.09	0.08
Combined $u(T_{90})$ (mK)	1.65	0.18	0.17	0.24	0.62	0.14	0.17	0.31

microwave measurements recorded in the proximity of a fixed point, and the corresponding estimates of T_{90} were obtained using the R_{90} values in table 2. For these estimates, the typical [33] sensitivity factors dT/dR listed in the same table 2 were used to account for the small differences between the experimental and the calibration values of T_{90} . At 161 K, the same procedure was not possible because the Xe cell previously constructed and characterized at INRiM [34] was not available, and the T_{90} estimate was necessarily based on the $W_{90}(T_{90})$ data reported in table 3 which were used to calculate the calibration coefficients of the deviation function (12) in [27] defined for the subrange 3.3.1.1, i.e. between the triple point of neon and the triple point of water (TPW).

From the data in tables 2 and 3, the comparison of the results of the 2018 and 2020 calibrations can be used to assess the stability of the thermometers and the overall combined effects of thermal cycling, transfer and handling back and forth between the calibration and measuring laboratories over a time span of three years.

From such a comparison, relevant changes are evident at 13.8 K with an increase of the resistances of RS144-01 and RS158-04 respectively equivalent to 6.3 mK and 3.2 mK. In addition to drifts resulting from thermal cycling and handling, these large variations may be partially attributed to the different calibration procedures used in 2018 and 2020, i.e. the comparison with a RIRT previously calibrated against an interpolating constant-volume gas thermometer in 2018 and the direct realization of the triple point of equilibrium hydrogen in 2020, with the former calibration having a larger uncertainty and the latter being possibly affected by thermal leakages which can affect the quality of the realized fixed points' plateaux. Also, the observed variations of the cSPRTs resistances near the TPW were found to be relevant, equivalent to as much as 2.4 mK for RS158-04. For all the other fixed points and temperatures in the range between 25 K and 161 K, the temperature equivalent stability of the cSPRTs was better than 0.7 mK for RS144-01 and 0.3 mK for RS158-04. Given these observations, the evaluation of the T_{90} temperatures for this work was obtained by the arithmetic mean of the 2018 and 2020 calibrations results for each cSPRT, and a specific uncertainty contribution, dubbed 'cSPRTs drifts' was included in the overall uncertainty budget of T_{90} discussed in section 3.3 and listed in table 4. This contribution was calculated assuming a rectangular distribution bounded by the maximum observed variation, between 2018 and 2020, of the resistances R_{90} of each cSPRT.

3.2. Thermometry and thermal gradients of RIGT apparatus

When mounted inside the cryostat employed for RIGT measurements (see figure 4), the electrical resistances of the cSPRTs were determined using an AC resistance bridge (Automatic Systems Laboratories, mod. F18) by measuring their ratio to the resistance of a thermostatted standard reference R_s (Tinsley mod. 5685A) chosen within a set comprising of 1 Ω , 10 Ω and 25 Ω nominal values, respectively used for the measurements at 13.8033 K and 24.5561 K, 54.3584 K and 83.8058 K, and 161.4060 K. An accurate estimate of the resistance of these reference standards, as needed for the determination of the cSPRTs resistance and therefrom T_{90} , was obtained by measuring their ratio, using the AC bridge, to a 10 Ω transfer standard of the same type previously calibrated with uncertainty in the order of 1 ppm by ratio comparison to a national primary standard maintained by the electrical metrology group of INRiM. The AC current I supplied by the bridge to the cSPRTs was set equal to: 1 mA for measurements performed at temperatures above the triple point of O_2 ; 2 mA for measurements near the Ne triple point; 5 mA for measurements at the e- H_2 triple point. For each RIGT measurement isotherm, the self-heating of both cSPRTs was evaluated, both in vacuum and with gas in the experimental vessel, by repeated measurements at I mA and $I/\sqrt{2}$ mA, followed by extrapolation to zero current.

As mentioned in the previous section, for all RIGT measurements other than those made near 161 K, the zero current resistance R of each cSPRTs was compared with the corresponding R_{90} measured during a nearby fixed point calibration. The resulting $(R - R_{90})$ differences, typically less than 20 mK, were multiplied by the sensitivity factor dT/dR in table 2, and finally added to the exact reference value T_{90} of the fixed point. For measurements around 161 K, T_{90} was instead obtained from the reference and deviation functions of ITS-90, for the subrange '3.3.1.1', defined by the W_{90} values listed in table 3.

In order to associate a single estimate of T_{90} from the readings of two cSPRTs, their mean was calculated for each RIGT measurement point. In doing so, any statistically relevant difference between the two cSPRTs indicates the presence of a thermal gradient across the experiment and must be accounted for as an additional uncertainty contribution. This is listed as *thermal gradient* in table 4 and evaluated assuming a rectangular distribution bounded by the two different cSPRTs readings. As shown in figures 3 and 4, the cSPRT dubbed RS144-01 is located in the top end of the cavity and thus closer than

RS158-04 to the 2nd stage of the cryocooler, which is supposed to reach the lowest temperature when the apparatus is in operation. Therefore, a negative temperature gradient $\Delta T = (T_{90,144} - T_{90,158})$ was generally expected. This expectation was confirmed with sporadic exceptions for measurements performed in vacuum. The values of ΔT were found to vary depending on T_{90} , and more slightly, depending on the thermometric gas (He or Ne) and the calibration data set considered (2018 or 2020). In both helium and neon, ΔT was the largest for measurements near 161 K, with $\Delta T \sim -2.8$ mK and $\Delta T \sim -0.8$ mK respectively. ΔT further increased to as much as -26 mK at 273 K when gas was filling the apparatus, though it was only -1 mK when the apparatus was evacuated at the same temperature. These observations indicate that large negative thermal gradients set up in the apparatus by heat conduction, through the gas, from the electrical heaters used to contrast the cooling power of the cryocooler. Between 83 K and 25 K, the amplitude of ΔT decreased from -0.8 mK to -0.3 mK. At 14 K, the thermal gradient was as large as $\Delta T \sim -1.5$ mK with a corresponding relevant contribution to the uncertainty of the determination of T_{90} .

3.3. T_{90} uncertainty budget

The uncertainty budget for the determinations of T_{90} is summarized in table 4, where the most relevant sources and contributions are listed for each RIGT measurement reference temperature. A more detailed, commented uncertainty budget is available in the electronic supplement (<https://stacks.iop.org/MET/17/025008/mmedia>).

For clarity and brevity, a single entry in the first row of table 4, dubbed *calibration uncertainty* is used to report the combined uncertainty from a large number of sources which contributed to the 2018 and 2020 calibration of the cSPRTs. These contributions include the uncertainty of the realization of fixed points or ITS-90 at INRiM and the resistance measurements in the calibration laboratory. The larger contribution affecting the measurements at 13.8 K with He reflects the larger uncertainty of the 2018 calibration realized by comparison with the wire scale maintained by a reference RIRT. Also, for measurements near 161 K in both He and Ne, where the calibration involves the reference and deviation functions of ITS-90, uncertainty includes propagation from the calibration fixed points and type 1 and type 3 non-uniqueness [35, 36]. For the other RIGT measurements at temperatures near the triple points of neon, oxygen and argon, the calibration uncertainty is in the order of 0.1 mK.

The uncertainty contribution in row 2 of table 4 refers to the additional uncertainty of resistance measurements taking place in the RIGT laboratory. This is always less than 0.1 mK and is included in table 4 for completeness.

The entries in row 3 of table 4 account for the thermal gradient ΔT resulting from the different readings of the two cSPRTs installed on the resonator, which was found to be particularly relevant at 13.8 K and 161 K, as commented in the previous section. The corresponding uncertainty contributions assume a rectangular distribution and were estimated as $\Delta T/(2\sqrt{3})$.

The last relevant contribution to the combined uncertainty of T_{90} , previously discussed in section 3.1 and reported as ‘*thermometers’ drifts*’ in table 4, accounts for the consequences of applying, for the evaluation of T_{90} , the results of the 2018 calibration accomplished before starting the RIGT measurements or, alternatively, the results of the calibration carried out in 2020 after their conclusion. This contribution dominates the combined uncertainty of T_{90} and therefore that of our determination of $(T - T_{90})$ at 13.8 K. Again, the corresponding uncertainty contributions listed in table 4 assume a rectangular distribution spanning the variation of T_{90} caused by the alternative application of the 2018 and 2020 calibration results.

4. Determination of the effective isothermal compressibility of the resonator as a function of temperature

In this section we discuss the methods, procedures and results upon which is based our determination of the effective compressibility κ_{eff} appearing in equations (1) and (6) to account for the elastic distortion of the microwave resonator under pressure. As the name states, κ_{eff} is an *effective* quantity defined by the elastic response of the resonator being a composite object rather than a property of the material (copper) by which it is constructed.

In the approach followed here, an estimate of the effective isothermal compressibility $\kappa_{T,\text{eff}}$ at the reference temperature of 273.16 K was obtained by microwave measurements in He with a procedure similar to that used for RIGT (section 4.2), while the temperature dependence $\kappa_{T,\text{eff}}(T)$ over the whole range of interest for this work was obtained by an extrapolation procedure previously described and discussed in [37]. This procedure exploits the fundamental relation between the temperature dependence of the adiabatic compressibility κ_s and the change in volume V with temperature T , as firstly expressed by Grüneisen in 1912 [38]:

$$\frac{\kappa_s(T)}{\kappa_s(T_0)} = \left(\frac{V(T)}{V(T_0)} \right)^\delta, \quad (11)$$

where T_0 is a reference temperature, and δ is the so-called Anderson–Grüneisen parameter, which is set to be constant as a basic assumption of the model [38]. Recently, it was shown that this assumption is sufficiently fulfilled down to cryogenic temperatures for the literature data of copper [37]. Consequently, if a determination of δ around room temperature is available, it can be used for the sake of a reliable extrapolation of $\kappa_s(T_0)$ to low temperature using equation (11). In this work, the determination of δ is based on RUS estimates of the bulk modulus of several copper samples (section 4.3). We remark that equation (11) holds for the adiabatic compressibility κ_s , while in RIGT the isothermal compressibility κ_T is needed. The link between these properties is given by a fundamental thermodynamic relation [38]

$$\kappa_T(T) = \kappa_s(T)(1 + \gamma\alpha_V T), \quad (12)$$

with

$$\gamma = \alpha_V / (\kappa_S c_p \rho), \quad (13)$$

where γ is called Grüneisen parameter, α_V is the volumetric thermal expansion coefficient, c_p the specific heat capacity at constant pressure, and ρ is the density. A combination of equations (11) and (12) at the reference temperature at 273.16 K leads to:

$$\kappa_T(T) = \kappa_S(273.16 \text{ K}) \left(\frac{a(T)}{a(273.16 \text{ K})} \right)^{3\delta} (1 + \gamma \alpha_V T), \quad (14)$$

where $a(T)$ is the internal radius of the microwave resonator at temperature T . At this point, a link between the properties of the material and the properties of the measuring artefact has been established because the determination of the cavity radius as a function of temperature, and therefrom the determination of α_V can be performed *in situ* via microwave measurement of the vacuum resonance frequencies (see section 4.1). Finally, the effective compressibility of the resonator $\kappa_{T,\text{eff}}(T)$ is obtained by the effective compressibility $\kappa_{T,\text{eff}}(273.16 \text{ K})$ previously converted to $\kappa_{S,\text{eff}}(273.16 \text{ K})$ using equation (12). This leads to the final expression:

$$\kappa_{T,\text{eff}}(T) = \kappa_{S,\text{eff}}(273.16 \text{ K}) \left(\frac{a(T)}{a(273.16 \text{ K})} \right)^{3\delta} (1 + \gamma \alpha_V T). \quad (15)$$

With the procedure described above, the specific compressibility of the artefact is obtained.

4.1. Determination of the thermal expansion of the microwave cavity

The fractional variation of the resonator radius as a function of temperature under vacuum conditions can be evaluated directly from microwave resonance frequency measurements to provide an estimate of the effective linear thermal expansion coefficient of the copper cavity $\alpha_L(T)$. For this purpose, in the experiments described here, two different analysis techniques, dubbed ‘local’ and ‘global’, were applied. The ‘local’ procedure consists in recording n successive temperatures and microwave frequencies $\{(T_n, \langle f_m \rangle_n)\}$ data pairs while the system—under vacuum—is slowly approaching the nominal temperature of each isotherm T_{iso} , i.e. one of T_{90} cryogenic fixed points under examination. The average resonance frequency of each mode at thermal equilibrium $\langle f_m \rangle_{\text{ref}}$ is selected as a reference value and the points $\{(T_n - T_{\text{iso}}, \langle f_m \rangle_n / \langle f_m \rangle_{\text{ref}})\}$ are fitted with a polynomial function $a_0 + a_1(T - T_{\text{iso}}) + a_2(T - T_{\text{iso}})^2$. The inclusion of a second order term is only necessary if the fit residuals show a systematic variation with T , indicating a relevant variation of temperature during thermalization. The absolute value of the fitted parameter a_1 , with its uncertainty, is assumed as an estimate of α_L at the temperature T_{iso} . To speed up the data acquisition, only the frequencies of the TM11 and TM12 modes are used for this calculation. Since the temperature of the cavity fluctuates slightly around T_{iso} during ‘isotherm’ data acquisitions, due to imperfections in the temperature control system, local values of α_L are used to correct single experimental modes frequencies values at the nominal T_{90} temperature of the actual isotherm.

The ‘global’ procedure for the determination of the volume thermal expansion coefficient at zero pressure $\alpha_V(T) = 3\alpha_L(T)$ aims at assessing a functional form for the representation of this parameter over the wide temperature range comprised between 9 K and 290 K, as necessary for the evaluation of the volume compressibility coefficient discussed above. The experimental vessel was initially thoroughly evacuated at 161 K, then the heaters were turned off and the cryostat allowed to reach the minimum operating temperature around 9 K. The data acquisition software and hardware were switched to a ‘fast mode’ configuration, with a new temperature reading from a single thermometer (RS158) available every 60 s and resonance data collected only for TM11 mode. The cryostat was then switched off, and paired temperature and frequency values $\{(T_n, \langle f_m \rangle_n)\}$ collected while the system was reverting towards ambient temperature at a mean rate of 40 mK per minute. The resulting dataset $\{(T_n, -\ln(\langle f_m \rangle_n))\}$ was fitted with a twelfth order polynomial function $\sum_{l=0}^{12} a_l T^l$ over the whole temperature range, finding that the experimental TM11 frequency as a function of T differed from the fitted curve less than 0.08 ppm. The first derivative with respect to T of this polynomial provides an estimate of the aimed function $\alpha_L(T)$ with an estimated overall relative uncertainty of 3%.

4.2. Determination of $\kappa_{T,\text{eff}}(T)$ by microwave measurements in He at 273.16 K

By definition, at the TPW the thermodynamic temperature T and the temperature $T_{90} = 273.16 \text{ K}$ can be assumed to be equal within the low relative uncertainty (3.7×10^{-7}) of the CODATA 2017 adjusted value of the Boltzmann constant k . With this premise, equation (1) can be rearranged as

$$n(p, T_{90} = 273.16 \text{ K}) \frac{\langle f_m(p, T_{90} = 273.16 \text{ K}) \rangle}{\langle f_m(0, T_{90} = 273.16 \text{ K}) \rangle} = (1 + \kappa_{T,\text{eff}} p), \quad (16)$$

where $\langle f_m(p, T_{90} = 273.16 \text{ K}) \rangle$ are the microwave frequencies acquired at the TPW temperature. Equation (16) indicates that an estimate of $\kappa_{T,\text{eff}}(273.16 \text{ K})$ can be obtained from a linear fit, if the refractive index of the gas is accurately known as a function of pressure at $T_{90} = 273.16 \text{ K}$. This is in fact the case for helium, given the accuracy of the *ab initio* calculation of $n(p, T)$, as discussed in section 5. We remark that at 273 K the performance of the apparatus, in terms of temperature stability and uniformity and accessible density working range, was inferior to that achieved at lower temperatures. For example, the thermal gradient across the cavity indicated by the cSPRTs was as large as 26 mK and the maximum working pressure was limited to 500 kPa due to the characteristics of the experimental vessel. In spite of these limitations, microwave measurements in He at 13 pressures in the range between 60 kPa and 500 kPa were recorded at temperatures near the TPW. To assess a possible hysteretic component in the deformation of the resonator under pressure, measurements at each pressure along the isotherm were repeated twice, first by increasing the pressure from vacuum up to 500 kPa and then, in reverse order, decreasing the pressure along the same sequence. A comparison of the microwave frequencies in

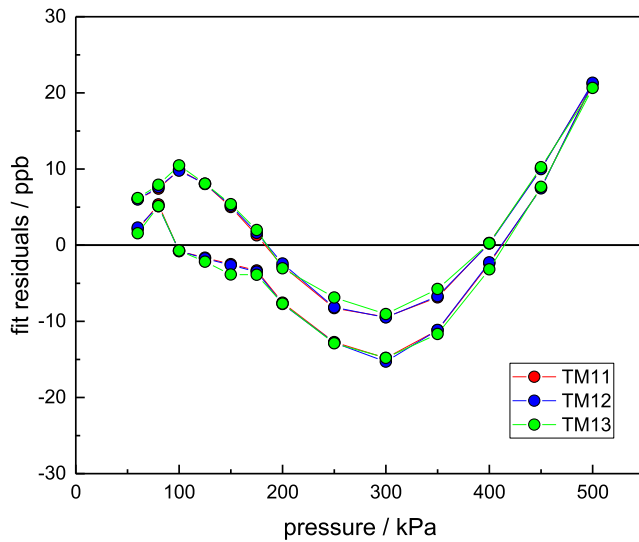


Figure 10. Relative deviations of the refractive index data scaled by microwave frequency ratios in equation (17) from a fitted linear model as a function of pressure. The lines connecting the points serve as a guideline for the eye. The intercept at $p = 0$ was adapted to the data by the fit procedure. The fitted slope provides an estimate of the effective isothermal compressibility $\kappa_{T,\text{eff}}$ of the resonator at 273.16 K.

vacuum recorded at the start and at the end of the sequence showed their consistency at the level of a few ppb.

Among the various mathematical combinations of the raw microwave data which may be used for the estimate of $\kappa_{T,\text{eff}}(273.16 \text{ K})$, the following

$$\left\{ \left(p_j, n(p_j, 273.16 \text{ K}) \frac{\langle f_m(p_j, 273.16 \text{ K}) \rangle}{\langle f_m(0, 273.16 \text{ K}) \rangle} \right) \right\} \quad (17)$$

can be fitted with a linear model $a_0 + a_1 p$ with $a_1 = \kappa_{T,\text{eff}}(273.16 \text{ K})$. Figure 10 shows the residuals for this linear fit, which essentially estimates $\kappa_{T,\text{eff}}$ implementing an extrapolation to zero pressure.

Since the limited pressure range does not justify the addition of a second order term to the model, the origin of the residual observed dependence on pressure remains unknown. We suspect an error in pressure measurement, but a close examination of data did not reveal any anomaly.

An alternative method of analysis is based on the data combination:

$$\left\{ \left(p_j, n(p_j, 273.16 \text{ K}) \frac{\langle f_m(p_j, 273.16 \text{ K}) \rangle}{p_j \langle f_m(0, 273.16 \text{ K}) \rangle} \right) \right\} \quad (18)$$

which can be fitted with the hyperbolic model $a_0/p + a_1$. Again, a_1 provides an estimate of $\kappa_{T,\text{eff}}(273.16 \text{ K})$, this time by implementing an extrapolation to infinite pressure, a complementary condition if compared to the linear model. Table 5 summarizes the results obtained by these two alternative models. It is evident from the data in table 5, where the uncertainties account for the combined effect of the contributions of the extrapolation and the imperfect determination of pressure, that the two procedures give barely compatible results with a coverage factor $k = 1$. Therefore, a uniform distribution is assumed appropriate to combine the two results

into a single value for $\kappa_{T,\text{eff}}$ corresponding to the arithmetic mean of the two estimates, equivalent to $\kappa_{T,\text{eff}}(273.16 \text{ K}) = 2.498(10) \times 10^{-12} \text{ Pa}^{-1}$.

4.3. RUS determination of $\kappa_S(T)$ of electrolytic tough pitch copper between 233 K and 323 K

Equation (11) shows that for a determination of the Anderson–Grüneisen parameter δ both the temperature dependence of the density $\rho(T)$ and that of the adiabatic compressibility $\kappa_S(T)$ of the material comprising the resonator are needed. For this purpose, three parallelepipedic samples of Cu-ETP copper provided by LNE, with nominal dimensions of $(15 \times 11 \times 10) \text{ mm}$, were weighed and dimensionally characterized. These preliminary operations led to the estimate of the density of the copper samples $\rho(293 \text{ K}) = 8925(20) \text{ kg m}^{-3}$. Using the determination of the thermal expansion $\alpha_V(T)$ described in the previous section, the temperature dependence of the density was determined.

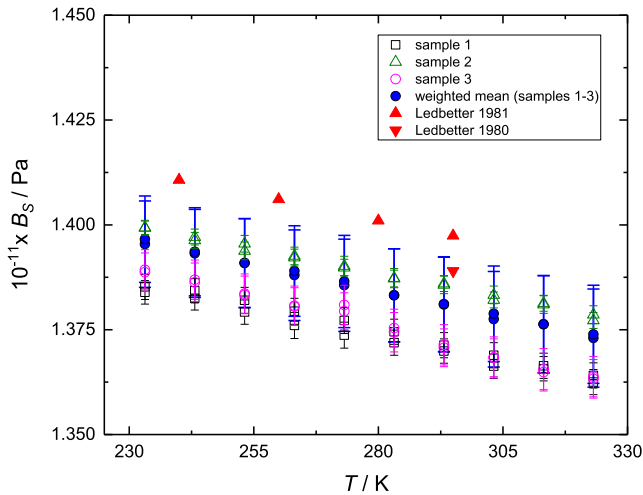
For the determination of $\kappa_S(T)$, the bulk modulus $B_S = 1/\kappa_S$ of Cu-ETP copper was estimated using the methods and techniques of RUS [39, 40], which requires the measurement of the normal-mode resonance frequencies of free vibration of a solid sample of known mass and verified shape. RUS measurements between 233 K and 323 K have been performed in 10 K steps for three samples at PTB using the experimental setup and procedures previously described in [9, 41].

The determination of the bulk modulus from RUS frequencies is an inverse problem. It starts with a forward problem, i.e. the calculation of resonance frequencies of free elastic vibrations of a sample with given geometry, known mass density and elastic coefficients. The calculated frequencies are then compared with the measured spectrum. In an iterative process, the input parameters are then adjusted during each iteration step to minimize the error function, which is defined as the square sum of the differences between the calculated and measured frequencies. Except for some particularly simple cases, the calculation of resonance frequencies cannot be solved analytically, but it can be turned into an eigenvalue problem by the use of proper numerical methods. Based on the Rayleigh–Ritz method, Visscher *et al* [42] established for simple sample shapes (parallelepiped blocks, spheres and cylinders) a computational scheme for the free vibration of a sample with anisotropic properties. The inverse problem is a multi-dimensional non-linear optimization problem. The Levenberg–Marquardt method may be considered as the standard non-linear optimization method, which in conjunction with the Rayleigh–Ritz method has been implemented in the rectangular parallelepiped resonator (RPR) code designed by Migliori *et al* [40]. For estimating the uncertainty of the solution of the inverse problem, the results obtained with both the RPR code and a finite element method were compared for all test samples.

In figure 11 the temperature dependent results $B_S(T)$ for the different samples are shown. The uncertainty bars are derived from the uncertainty of the measurement (repeatability of multiple measurements of the same sample) and the uncertainty of the density measurement mentioned before. Furthermore Monte-Carlo simulations with varied peak positions have

Table 5. Fitted estimates of the effective isothermal compressibility $\kappa_{T,\text{eff}}$ of the microwave cavity at 273.16 K.

	Volume compressibility $3 \times 10^{12} \times \kappa_{T,\text{eff}} \text{ Pa}^{-1}$	Absolute uncertainty volume compressibility $3 \times 10^{12} \times u(\kappa_{T,\text{eff}}) \text{ Pa}^{-1}$	Linear compressibility $10^{12} \times \kappa_{T,\text{eff}} \text{ Pa}^{-1}$	Relative fitting uncertainty $u_r(\kappa_{T,\text{eff}})$
Linear fit (17)	7.545	0.039	2.515	0.005
Hyperbolic fit (18)	7.444	0.039	2.481	0.005
Combined estimate	7.495	0.029	2.498	0.004

**Figure 11.** Determination of the adiabatic bulk modulus of copper by RUS. For comparison literature data from Ledbetter 1980 [43] and Ledbetter 1981 [44] are shown.

been performed. This leads to a relative standard uncertainty between 0.2% and 0.3%.

In the fit routine described in [40, 42], for poly-crystals mostly the isotropic case (two free parameters) is used to describe the resonance frequencies. While this model works impeccably for tungsten carbide samples [9], a well-known problem of copper is that, depending on the quality of the copper and copper alloys [37], an increased grain size may lead to a certain anisotropy. To account for this effect, it is necessary to consider a possible, lower microscopic crystal symmetry. For this reason, the resonance frequencies have been fitted with a different number of free fit parameters (the number increases with decreasing symmetry), and the fit residuals have been evaluated as an indicator of the fit quality. It was clearly visible that for all specimens, the isotropic evaluation had too large fit residuals, and the isotropic results deviated significantly from the expected value estimated from elastic-constant data published in standard textbooks. However, if the evaluation is performed for cubic symmetry (three free parameters) and orthogonal symmetry (nine free parameters), the fit residuals are much smaller, and the bulk modulus and the other elastic constants become consistent with literature data within the uncertainty estimates. To account for a certain model ambiguity, the final result is a weighted mean of the results obtained for the different samples and evaluated with three and nine free parameters. The final relative standard uncertainty for the bulk modulus in the temperature range between 233 K and 323 K is about 0.8% (see figure 11). A linear fit through the data leads to estimates of the intercept $a_{B_s} = 1.453(7) 10^{11} \text{ Pa}$ and the slope

$b_{B_s} = -2.47(15) 10^7 \text{ Pa K}^{-1}$ and therefore to the estimate $B_s(273.16 \text{ K}) = 1.386(11) 10^{11} \text{ Pa}$. A comparison with literature values of B_s [43, 44] is plotted in figure 11. Unfortunately in [43, 44] no uncertainties are stated. In [43] an intensive study has been performed to extract a value for B_s at 295 K whereby the focus of [44] was on the temperature dependence. Therefore the discrepancy between two values published at 295 K can give a rough estimate of the uncertainty of B_s in [44]. The relative difference between the B_s value at 295 K published in [43] and the actual value is about 0.6% and therefore well inside the standard uncertainty estimates of this work. A comparison with the slope b_{B_s} published in [44] shows a difference of $0.2 10^7 \text{ Pa K}^{-1}$, in good agreement with the value stated above.

In summary, the results of the RUS experiment together with data on thermal expansion, specific heat capacity [22] and density can be used for the determination of the Anderson–Grüneisen parameter δ and of the Grüneisen parameter γ according to equations (11) and (13) respectively. A mean value in the temperature range between 250 K and 295 K, where the linear assumption of the bulk modulus is justified, leads to $\delta = 3.6(2)$ and $\gamma = 2.00(6)$. The fitted coefficients a_{B_s} and b_{B_s} , together with equation (12), lead to the final RUS estimate of the isothermal linear compressibility $\kappa_{T,\text{RUS}}(273.16 \text{ K}) = 2.469(19) 10^{-12} \text{ Pa}^{-1}$.

4.4. Comparison of microwave and RUS determinations of the compressibility and temperature extrapolation

As already mentioned, the effective compressibility of the resonator is a property of the assembled artefact that is mainly determined by the elastic properties of the comprising material, but may still be significantly influenced by the assembly. Therefore, the compressibility of the assembled artefact must be preferred as the most reliable estimate of the elastic response of the resonator. Nevertheless, the difference between the compressibility estimate obtained from microwave measurement at 273.16 K and the estimate determined by RUS is a useful indicator of the quality of the resonator assembly (misalignment, gaps between the two hemispheres etc). In [5] the determinations of the compressibility from microwave measurements along an isotherm have been compared with literature data on OFHC copper having 1.5% uncertainty. Within this uncertainty range the agreement was found to be within one percent. In the case of the capacitors used for DCGT the deviations between two capacitors, which are in principle identically manufactured and assembled, is on the level of 0.8%, as discussed in [37].

In principle, especially for DCGT, a suitable design of the apparatus can be conceived to minimize the assembly effects

Table 6. Effective isothermal length compressibility of the resonator. The values κ_{eff} are extrapolated from the experimental microwave determination $\kappa_{T,\text{eff}}(273.16 \text{ K})$ and were used for the final evaluation of the thermodynamic temperature in this work. For comparison, the listed κ_{RUS} values are extrapolated from a RUS determination $\kappa_{T,\text{RUS}}(273.16 \text{ K})$. The temperature variations $\kappa_{\text{RUS}}(T)$ and $\kappa_{\text{eff}}(T)$ are shown in figure 12.

$T_{90} \text{ K}$	$10^{12} \times \kappa_{\text{eff}} \text{ Pa}^{-1}$	$10^{12} \times \kappa_{\text{RUS}} \text{ Pa}^{-1}$
13.8058	2.357(10)	2.330(20)
24.5561	2.357(10)	2.330(20)
54.3554	2.362(10)	2.335(20)
83.8058	2.374(9)	2.347(19)
161.4061	2.420(9)	2.392(19)

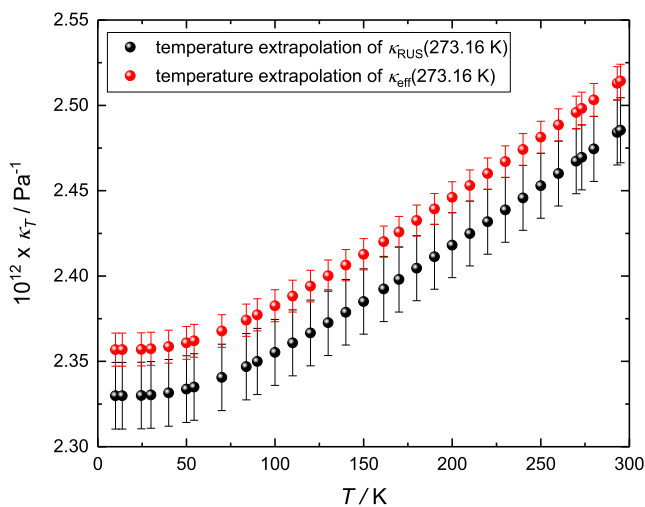


Figure 12. Comparison and extrapolation to low temperature of RUS and microwave determinations of the isothermal compressibility.

[9] but the *in situ* measurement of the compressibility has the advantage that all non-idealities are captured by a single experimental determination. In the present work, the relative difference between $\kappa_{T,\text{RUS}}$ and $\kappa_{T,\text{eff}}$ is about 1.5%. Within their combined standard uncertainty of about 0.9%, $\kappa_{T,\text{RUS}}$ and $\kappa_{T,\text{eff}}$ are consistent, and their difference is well inside the possible range of variation of this parameter. As discussed in the former sections, the value $\kappa_{T,\text{eff}}(273.16 \text{ K})$ is transferred via equation (12) to $\kappa_{S,\text{eff}}(273.16 \text{ K}) = 2.43(7)10^{-12} \text{ Pa}^{-1}$. This is the starting value for the extrapolation according to equation (15). Using the input from the thermal expansion measurement discussed in section 4.1 as well as δ and γ derived in section 4.3, the extrapolation to 9 K (the low temperature end of the thermal expansion measurement) can be performed. The uncertainties associated to this extrapolation are determined by the uncertainties of the input parameters, therefore a Monte-Carlo simulation was performed to assess the individual uncertainties as a function of temperature. The final resulting determinations of κ_{eff} and κ_{RUS} at the reference temperature of the isotherms and their uncertainties are listed in table 6. In addition, the temperature dependent length compressibility $\kappa_{\text{eff}}(T)$ is shown in figure 12 together with an extrapolation of $\kappa_{\text{RUS}}(T)$ for comparison.

Table 7. Synopsis of the experimental measurement plan.

Reference temperature $T_i \text{ (K)}$	n of pressure points p_j and pressure range in kPa	Thermometric gas
13.8033	9 points; $50 \leq p_j \leq 130$	He
24.5561	9 points; $65 \leq p_j \leq 200$	He
54.3584	13 points; $40 \leq p_j \leq 350$	He, Ne
83.8058	13 points; $60 \leq p_j \leq 320$	He, Ne
161.405 96	8 points; $40 \leq p_j \leq 380$	He, Ne
273.16	13 points; $60 \leq p_j \leq 500$	He

Finally, we remark that the validity of the procedure for the determination of $\kappa_{T,\text{eff}}$ discussed above is based on two assumptions: (i) that the elastic response of the resonator must be only slightly anisotropic; (ii) that the possible small deviations from isotropicity must remain the same at all temperatures. From the presented results, the consistency of the microwave and RUS determinations of κ_{eff} at one particular temperature, i.e. 273.16 K, supports the validity of the first assumption. The very slight pressure variations of the shape factors presented in figure 9, section 2.4, for two quite different temperatures (25 K and 83 K), supports the second assumption.

5. Microwave determination of the thermodynamic temperature

5.1. Measurement procedure

The acquisition of microwave resonance frequencies $\langle f_m(p_{j,i}, T_i) \rangle$ was organized to proceed in nearly isothermal conditions in proximity of the reference temperatures T_i chosen to correspond to ITS-90 fixed points. For each isotherm, resonances were recorded and fitted at several pressures $p_{j,i}$, as summarized in table 7.

Before the start of each isotherm, the experimental vessel was thoroughly evacuated while the resonator thermalized towards the targeted temperature setpoint, a process requiring up to 72 h to be completed. Microwave resonance frequencies were recorded during the slow approach to the setpoint temperature for the ensuing estimate of a ‘local’ linear thermal expansion coefficient, as discussed in section 4.1. Upon attainment of a satisfactory thermal equilibrium by the cavity, with daily temperature fluctuations below $\pm 3 \text{ mK}$, an automated data acquisition procedure—comprising two thermometers reading, two pressure transducers polling and six mode frequencies scanning every 180 s—was triggered and let to run on for at least 12 h. The same procedure was applied after each scheduled variation of the gas pressure, with the additional activation of a pressure PID control and a manually operated calibration of the two pressure quartz transducers against the pressure balance. An ordinary measurement sequence along an isotherm proceeded by increasing the experimental pressure in steps from vacuum to the maximum pressure set for each isotherm. In order to check the reproducibility of measurements, especially in the lower pressure investigated range, measurements were occasionally repeated. In this respect, the 273.16 K isotherm used for the determination of κ_{eff}

represented an exception, since every pressure point was repeated twice.

As the final result of the measurement campaign, a recorded set of at least 150 fitted resonance frequencies for each microwave mode at each investigated thermodynamic state was available. These experimental records were corrected to compensate for the slight pressure and temperature differences of each individual measurement within an homogeneous time series from the reference (p_{ji} , T_i) values. The correction involved the experimental estimate of the thermal expansion coefficient discussed above and the *ab initio* calculated virial expansion of the refractive index. The effectiveness of the correction procedure was verified on very long time series, where long term fluctuations of temperature caused frequency fluctuations outside the noise band. It was observed that, satisfactorily, the correction algorithm completely eliminated the observed systematic trends and did not amplify the random noise. Upon correction, frequency data in a time series were assumed to be associated to the same nominal pressure and temperature value and could be averaged to determine, for each microwave mode a single reference frequency value $f_m(p_{ji}, T_i)$. All these averaged, corrected data are available in the electronic supplement (<https://stacks.iop.org/MET/17/025008/mmedia>).

5.2. Determination of thermodynamic temperature from measurements in helium

For a microwave determination of the thermodynamic temperature, the quantities of interest for the analysis are the vacuum/pressure frequency ratios

$$r_m(p_{ji}, T_i) = \frac{\langle f_m(0, T_i) \rangle}{\langle f_m(p_j, T_i) \rangle}. \quad (19)$$

In equation (19), the frequencies $\langle f_m(0, T_i) \rangle$ can be determined by measuring the resonances of the evacuated cavity or, alternatively, by extrapolating to zero pressure the series of data collected at several pressures p_{ji} along an isotherm at temperature T_i . In the present study, these two alternatives typically differed by less than 5 ppb and the experimentally determined $\langle f_m(0, T_i) \rangle$ were preferably used for the evaluation of the ratios r_m in order to avoid the additional extrapolation uncertainty. The two recorded isotherms at 161.4 K in helium and at 54.4 K in neon, however, represented an exception to this rule, with relative differences between experimental and extrapolated vacuum frequencies in the order of 40 ppb. We suspect that these discrepancies were due to some undetected thermometry error occurred while measuring in vacuum, and we preferred the extrapolated vacuum frequencies, instead of those directly measured, for successive analysis.

Along the lines of the discussion in section 1.1, we now consider three different methods of analysis of a whole isotherm data set, each endowed with specific pros and cons.

The *direct single* (p , T) *state* determination treats the ensemble $r_m(p_{ji}, T_i)$ as a set of j independent determinations of T_i , one for each pressure state p_j , by solving numerically the implicit equation (1) with respect to the unknown T_i . We remark that this procedure, when applied to a fully

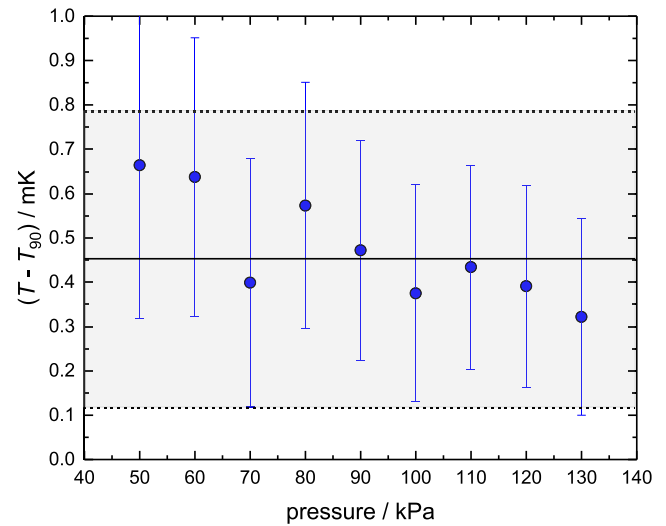


Figure 13. $(T - T_{90})$ results obtained using the *direct single-state* analysis for measurements in He at nine different pressure in the range between 50 kPa and 130 kPa at $T_{90} = 13.8054$ K. The error bars of each point are the standard uncertainty combined from several sources (table 8) of the determined thermodynamic temperature $T(p)$, and do not include the uncertainty of T_{90} which is intended only as a reference value. The black line represents the weighted mean of single pressure results. The grey shaded area is the uncertainty resulting from the quadrature sum of the contributions listed in table 8.

characterized and well-tuned apparatus, may be the method of choice for a practical primary temperature standard because it requires minimum experimental work for the determination of T , requiring just one measurement at a single pressure, which would be selected as that contributing the minimum uncertainty. However, this method has two main drawbacks. Firstly, the uncertainty of the gas pressure estimate propagates directly, with unit sensitivity factor, onto the uncertainty of the thermodynamic temperature; secondly, the method requires extremely accurate *ab initio* calculated properties of the thermometric gas, as they are currently available only for helium.

Figure 13 illustrates the $(T - T_{90})$ results obtained using the single-state analysis of microwave measurements in He at 13.8 K and nine different pressures between 50 kPa and 130 kPa. Remarkably, these determinations are consistent at all pressures. The complete set of results was averaged to provide a single weighted mean value for the isotherm.

The implementation of a second method of analysis of a set of microwave data, previously referred to as *ideal gas extrapolation* and discussed in section 1.1, is based upon equation (6) and does only require a theoretical or experimental independent determination of the molar polarizability ($A_\epsilon + A_\mu$) of helium in equation (3), as available from recent extremely accurate calculations and measurements of its electrical contribution A_ϵ [45–47] and more dated calculations and measurements of its magnetic contribution A_μ [48–50]. However, closely sampled data along an isotherm, over an extended pressure range, are needed to obtain sufficiently precise fitted parameters. Various *hybrid* extrapolation procedures [2] have been formulated to overcome specific experimental contingencies. Our apparatus, for example, is strongly limited by the experimental vessel which is rated for a maximum

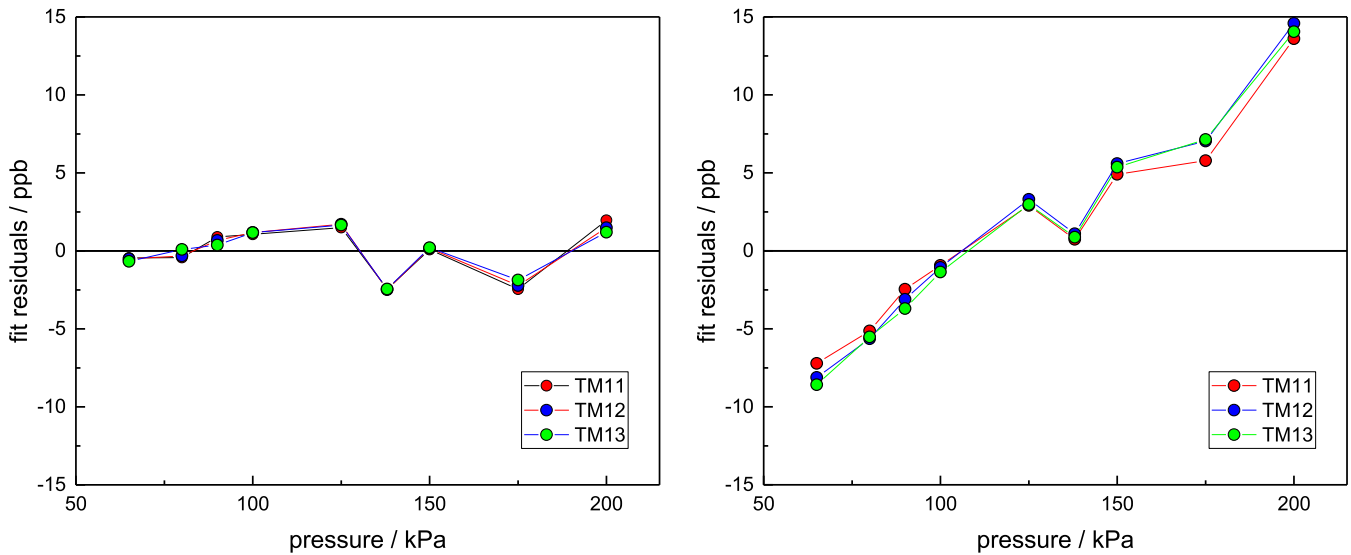


Figure 14. Comparison of two different extrapolations to zero pressure of refractive index data in He at 24.5 K. (Left plot) Residuals of a linear fit to microwave data prepared using equation (20). The fitting procedure adjusts both the zero-pressure intercept h_0 and the slope h_1 compensating for systematic errors in pressure measurements and vacuum frequencies. (Right plot) Residuals of a linear fit to microwave data prepared using equation (21). The parameter h_0 is now fixed to unity, its physics-grounded value. In spite of the much larger residuals resulting by the constraint $h_0 = 1$, the uncertainty associated to the determination of h_1 decreases because the fit has one less degree of freedom.

working pressure of 500 kPa. As a consequence, due to the narrow investigated pressure range, the differences from unity of the squared resonance frequencies ratios $[r_m(p_{j,i}, T_i)]^2$ are too small to accurately estimate the non-linear-terms in equation (6) and provide inconsistent results depending on the order of the fitting polynomial. In order to increase our confidence in the extrapolation, it was thus necessary to apply corrections to the ratios $[r_m(p_{j,i}, T_i)]^2$ before fitting.

These corrections construct a new data set:

$$\left(p_j, \frac{\langle f_m(0, T_i) \rangle^2}{\langle f_m(p_j, T_i) \rangle^2} - B_n(T_i) p_j^2 - C_n(T_i) p_j^3 \right), \quad (20)$$

where the definitions of $B_n(T)$ and $C_n(T)$ are respectively given by equations (4) and (5) and their estimate uses accurate *ab initio* calculations of the second and higher order density and dielectric virial coefficients which are available for He [51–56]. It must be noted that while this work was in preparation more accurate calculations of B_ρ [57] and b_ε [58, 59] of He became available; however the impact of updating our determinations of T based on these new estimated properties is significantly lower than the uncertainty achieved by the present measurements.

The corrected squared frequency ratios in equation (20) can be fitted with a two-parameter linear model $r_m^2 = h_0 + h_1 p$. If the h_0 parameter is adapted to the data by the fitting procedure, the determination of h_1 is immune from a possible zero error in pressure measurement and partially compensates for any possible systematic error in the determination of the resonance frequencies in vacuum $f_m(0, T)$. The introduction of the ‘free intercept’ parameter h_0 has the general effect on the whole set of data to reduce systematic trends observable on fit residuals (see figure 14), at the cost of a moderate increase of the fitting uncertainty (see table 8).

Finally, we considered an alternative hybrid extrapolation method, in which h_0 is constrained to unity; in this case the data set subject to fitting becomes:

$$\left(p_j, \frac{\langle f_m(0, T_i) \rangle^2}{\langle f_m(p_j, T_i) \rangle^2} - 1 - B_n(T_i) p_j^2 - C_n(T_i) p_j^3 \right) \quad (21)$$

and the model reduces to a single fitted parameter $r_m^2 = h_1 p$. The uncertainty budget in table 8 shows that at all investigated temperatures this procedure determines T with the lowest combined uncertainty (at 54.4 K the difference with the free intercept extrapolation is negligible); however the fit residuals become larger and systematic compared to the ‘free intercept’ method (see figure 14) for the isotherm at 24.5 K.

We remark that the values of T_i obtained with the three alternative models discussed above are all mutually consistent within their combined standard uncertainties (see table 8). However, for the sake of their combination in a single result, the calculation of their weighted mean (also listed in table 8) does not appear a suitable estimator for two reasons. Firstly, it leads to an uncertainty estimate which is far too optimistic if compared to the uncertainty of each method. Secondly, the weighted mean is a reliable estimator only under the assumption that the probability distributions of each estimate would be independent and normally distributed with the same mean, which is certainly not our case because the three estimates are obtained from the analysis of the same experimental data and, as such, are fully correlated. Instead, we selected the most accurate estimates of T obtained using the constrained extrapolation of equation (21). These are highlighted in bold in the rightmost column of table 8, and are used as the source data of the $(T - T_{90})$ determinations listed in table 1 and plotted in figures 1 and 2.

Table 8. Uncertainty budget and $(T - T_{90})$ results for thermodynamic temperature determinations with helium using different methods of analysis. Selected weighted mean values of $(T - T_{90})$ in mK and the corresponding combined uncertainty $u(T)$ are listed in boldface type.

T_{90} (K)	Method of analysis	Uncertainty source (mK)					$T - T_{90}$ (mK)	Combined uncertainty $u(T)$ (mK)
		κ_{eff}	Modes' dispersion	Frequency noise or extrapolation	Pressure	Theoretical value of B_ρ of He [51]		
13.8033	Single state		0.06	0.19	0.18	0.16	0.45	0.31
	Equation (20)	0.02	0.04	0.27	0.08	0.32	0.75	0.43
	Equation (21)		0.06	0.08	0.08	0.18	0.67	0.22
						Weighted mean	0.62	0.17
24.5561	Single state		0.05	0.08	0.23	0.12	−0.68	0.28
	Equation (20)	0.06	0.07	0.19	0.13	0.25	−1.14	0.35
	Equation (21)		0.06	0.06	0.13	0.14	−0.69	0.22
						Weighted mean	−0.78	0.16
54.3584	Single state		0.45	0.21	0.51	0.11	−3.01	0.78
	Equation (20)	0.31	0.13	0.18	0.29	0.16	−3.25	0.50
	Equation (21)		0.26	0.11	0.29	0.11	−3.03	0.52
						Weighted mean	−3.12	0.33
83.8058	Single state		0.24	1.26	0.73	0.06	−4.27	1.64
	Equation (20)	0.71	0.20	0.53	0.45	0.11	−3.78	1.02
	Equation (21)		0.17	0.25	0.44	0.08	−4.25	0.90
						Weighted mean	−4.08	0.62
161.406	Single state		0.37	2.23	1.32	0.05	−5.38	3.65
	Equation (20)	2.55	0.22	0.86	0.86	0.08	−5.61	2.83
	Equation (21)		0.24	0.28	0.81	0.05	−5.33	2.70
						Weighted mean	−5.45	1.72

The uncertainty budgets in tables 8 and 9 and table 12, for He, Ne and combined He/Ne data respectively, list the mostly relevant contributions to the determination of T , i.e. those which are relatively larger than 1 ppm. In these budgets, the meaning of particular entries may vary depending on the thermometric gas employed and the analytical method used for data analysis. Particularly, the entries in column ' κ_{eff} ' refer to the uncertainty contribution of our imperfect determination of the effective compressibility; in general, this contribution increases proportionally with thermodynamic temperature and is lower for Ne, in reason of its larger polarizability. The contributions reported as 'modes' dispersion' refer to the systematic discrepancies between the thermodynamic temperature evaluations from the three most precise resonance modes that we selected for analysis, i.e. TM11, TM12 and TM13. The column entitled 'frequency noise or extrapolation' summarises type A uncertainties deriving from: (a) random noise in the frequencies determinations for the *single state* method, or (b) the overall statistical uncertainty deriving from frequency noise, pressure random fluctuations and fit residuals when *extrapolation* methods are concerned. The 'pressure' column accounts for the combined uncertainty of pressure measurement (type A and type B) for *single state* method, or for the type B uncertainty in pressure measurements when referring to *extrapolation* methods. Finally, in table 8, the uncertainty contribution of the *ab initio* calculated value of the second density virial of He from [51] is included. Very recently, a significantly improved calculation of this quantity became available [57]; we remark that the reduction of the corresponding uncertainty contribution will significantly reduce the overall uncertainty of future RIGT determinations of T , particularly at low temperatures.

5.3. Determination of thermodynamic temperature from measurements in neon

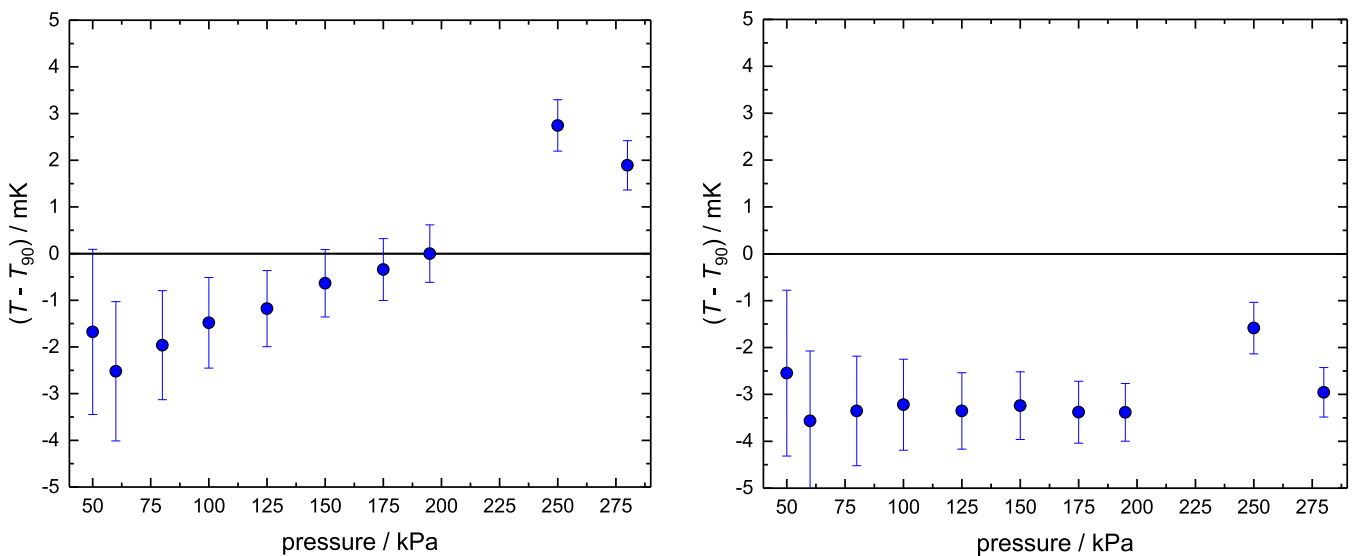
After completing measurements with helium, the apparatus was prepared for using neon as the thermometric gas. The cryocooler was switched off to let the experimental vessel and the microwave cavity slowly return to ambient temperature while being thoroughly evacuated (for a period of 20 days) in an attempt to eliminate any residual trace of helium gas from the apparatus. Successively, the cryocooler and the temperature control system were activated and the temperature stabilized near the triple point of oxygen. A measurement sequence was then triggered to explore roughly the same pressure ranges and pressure points as previously scheduled for He isotherms; this close repetition was crucial for a combination of helium and neon data, discussed in section 5.4.

In principle, the use of neon for a microwave determination of the refractive index, given its polarizability which is larger than that of helium by approximately a factor of two ($A_\epsilon^{\text{Ne}} \sim 0.99 \times 10^{-6} \text{ m}^3 \text{ mol}^{-1}$ versus $A_\epsilon^{\text{He}} \sim 0.52 \times 10^{-6} \text{ m}^3 \text{ mol}^{-1}$), is advantageous because it reduces the uncertainty contribution of the imperfect estimate of the compressibility and enhances the sensibility of the microwave frequencies as a function of density. In practice, we had to deal with the limited working pressure range of the apparatus and the minor accuracy, compared to He, of the *ab initio* calculations of the virial coefficients of Ne, which are crucial for a straightforward application of the analytical methods discussed in section 5.2.

The consequences of this issue are illustrated by the left plot in figure 15 which shows the *direct single state* determinations of T in neon at 54.4 K for ten pressures in the range between 50 kPa and 280 kPa. These determinations were first

Table 9. Uncertainty budget and $(T - T_{90})$ results for thermodynamic temperature determinations with neon using different methods of analysis. Weighted mean values of $(T - T_{90})$ and combined uncertainty of T are listed in boldface type.

T_{90} (K)	Method of analysis	Uncertainty source (mK)					$T - T_{90}$ (mK)	Combined uncertainty $u(T)$ (mK)
		$\kappa_{\text{eff}}(T)$	Modes' dispersion	Frequency noise or extrapolation	Pressure	Theoretical value of A_ε , A_μ and B_ρ of Ne [47, 60, 62]		
54.3584	Single state optimization	0.15	0.13	0.74	0.50	0.94	−3.23	1.31
	Equation (22)		0.10	1.17	0.29	0.13	−4.88	1.22
	Equation (23)		0.13	0.38	0.29	0.13	− 3.53	0.53
						Weighted mean	−3.68	0.46
83.8058	Single state optimization	0.34	0.23	0.69	0.72	1.14	−4.80	1.57
	Equation (22)		0.24	0.88	0.45	0.20	−5.29	1.09
	Equation (23)		0.26	0.27	0.45	0.20	− 4.82	0.71
						Weighted mean	−4.94	0.55
161.406	Single state optimization	1.13	0.55	1.00	1.44	0.83	−7.60	2.31
	Equation (22)		1.41	3.94	0.86	0.39	−8.83	4.44
	Equation (23)		0.56	0.89	0.86	0.39	− 7.57	1.81
						Weighted mean	−7.70	1.35

**Figure 15.** Direct single (p, T) state determinations of $(T - T_{90})$ in neon at 54.4 K. (Left plot) determination based on published [61, 63] estimates of the second density and dielectric virial coefficient of neon. (Right plot) determinations adjusted by an optimization procedure of the combination $(b_\varepsilon - B_\rho)$. In reason of its inconsistency in the isotherm data set, the datum at 250 kPa was excluded from the optimization procedure.

implemented using the best currently available⁵ sources of the thermodynamic [60] and electromagnetic properties of Ne [47, 61, 62]. The corresponding results were observed to be clearly pressure-dependent, suggesting that the theoretical estimate of the second density virial coefficient B_ρ of Ne [60] may not be sufficiently accurate for the present application.

⁵ While this work was in preparation improved estimates of the second dielectric virial b_ε of Ne became available [56, 57]. These new estimates do not change the systematic deviation displayed in the left plot of figure 15 because of the much smaller contribution to the refractive index of b_ε compared to the second density virial B_ρ .

Motivated by this evidence, we explored the possibility to use our experimental microwave data to determine, in addition to our estimate of the thermodynamic temperature T , also a revised estimate of B_ρ . This possibility is supported by the following observations: (i) the thermodynamic temperature T of the isotherm is unknown, but we are reasonably confident that all the experimental data at different pressure were acquired very nearly at the same temperature. Thus, when equation (1) is resolved with respect to T for several different pressures p_j , it is expected to provide the same solution for all pressures, apart from random experimental fluctuations. In other words, the slope of the plotted points in figure 15 should be

Table 10. Experimental adjusted estimates of $(b_\varepsilon - B_\rho)$ in neon at three thermodynamic temperatures T . The superscripts ‘calc’, ‘opt’ and ‘fit’ respectively refer to *ab initio* calculation [60, 61], single state optimization and linear extrapolation to zero pressure. The rightmost column lists the estimated values of B_ρ of Ne resulting from $(b_\varepsilon - B_\rho)^{\text{opt}}$ and calculated values of b_ε from [61].

T (K)	$(b_\varepsilon - B_\rho)^{\text{calc}}$ [60, 61] (cm ³ mol ⁻¹)	$(b_\varepsilon - B_\rho)^{\text{opt}}$ (cm ³ mol ⁻¹)	$(b_\varepsilon - B_\rho)^{\text{fit}}$ (cm ³ mol ⁻¹)	B_ρ^{opt} (cm ³ mol ⁻¹)
54.355	30.760	30.615 ± 0.042	30.595 ± 0.042	-30.666 ± 0.042
83.801	9.934	9.874 ± 0.017	9.874 ± 0.023	-9.924 ± 0.017
161.399	-5.531	-5.494 ± 0.011	-5.494 ± 0.063	5.429 ± 0.011

zero; (ii) in the virial expansion of the refractive index of equation (2), the coefficient B_n in equation (4) is in principle defined by the difference $(b_\varepsilon - B_\rho)$ with a prevalence of B_ρ in the definition because at all temperatures investigated for neon measurements $|B_\rho| \gg |b_\varepsilon|$.

We used a minimization procedure to adjust the combination $(b_\varepsilon - B_\rho)$, the merit function being the minimum slope of the line which fits the data $\{(p_j, T_j)\}$ generated applying the implicit equation (1) to each pressure point p_j . The result of this optimization process on data taken at 54.4 K in neon is shown in the right plot of figure 15. The values of T optimized by this procedure at 54.4 K, 83.8 K and 161.4 K and their uncertainties are listed in table 9, dubbed *single state optimization*. The corresponding optimized estimates of the combinations $(b_\varepsilon - B_\rho)$ are listed as $(b_\varepsilon - B_\rho)^{\text{opt}}$ in table 10.

As an alternative approach towards the determination of T and $(b_\varepsilon - B_\rho)$ with the hybrid extrapolation methods discussed in the previous section, a second order parameter h_2 must be added to the fitting model which becomes $r_m^2 = h_0 + h_1p + h_2p^2$ and $r_m^2 - 1 = h_1p + h_2p^2$ for the free- and fixed intercept method respectively. The application of this method requires the microwave data to be prepared by variants of equations (20) and (21), i.e. by correcting for a cubic term only:

$$\left(p_j, \frac{\langle f_m(0, T_i) \rangle^2}{\langle f_m(p_j, T_i) \rangle^2} - C_n(T_i) p_j^3 \right) \quad (22)$$

for the free intercept method, and

$$\left(p_j, \frac{\langle f_m(0, T_i) \rangle^2}{\langle f_m(p_j, T_i) \rangle^2} - 1 - C_n(T_i) p_j^3 \right) \quad (23)$$

for the fixed intercept method. The extrapolation procedures were applied to determine $(T - T_{90})$ at 54.4 K, 83.8 K and 161.4 K with the results and the uncertainties listed in table 9. Remarkably, all the $(T - T_{90})$ determinations obtained using neon as the thermometric gas were found to be consistent with the corresponding results in helium within their combined uncertainties, reinforcing our confidence that our experimentally based estimates of $(b_\varepsilon - B_\rho)$, and of B_ρ therefrom, may be sound and accurate. These estimates are listed in table 10 where $(b_\varepsilon - B_\rho)^{\text{opt}}$ refers to results adjusted by the single state optimization procedure, and $(b_\varepsilon - B_\rho)^{\text{fit}}$ refer to those obtained by fitting data in equation (22) with a linear model. For comparison, table 10 also lists $(b_\varepsilon - B_\rho)^{\text{calc}}$ calculated *ab initio* from [60, 61]. To assess a conservative estimate of the uncertainties to be attributed to our determinations

of $(b_\varepsilon - B_\rho)$, we assumed the calculated and adjusted values $(b_\varepsilon - B_\rho)^{\text{opt}}$ to be the limiting extreme points of a uniform probability density distribution. For the estimates $(b_\varepsilon - B_\rho)^{\text{fit}}$ the listed uncertainties are those resulting from the fit procedure.

Finally, from our lowest uncertainty results $(b_\varepsilon - B_\rho)^{\text{opt}}$, by subtraction of the calculated value of b_ε from [61] we obtain experimentally based estimates B_ρ^{opt} of the 2nd density virial coefficients of Ne at three thermodynamic temperatures T listed in the leftmost column of table 10. Any other more recent calculation of b_ε of Ne, like [58, 59], would have a negligible impact on the determination of B_ρ , given that $|B_\rho| \gg |b_\varepsilon|$.

The same fitting procedure described above for Ne data prepared using equation (22) can also be used to analyze He data to obtain an experimental estimate of the combination $(b_\varepsilon - B_\rho)^{\text{fit}}$ for this gas at five thermodynamic temperatures in the range spanning between 13.8 K and 161.4 K. In spite of their much larger uncertainty, these results may be of interest for the sake of a comparison with the theoretical calculation of the same properties. The results of this comparison are listed in table 11. By assuming either of the two recent calculations of b_ε of helium from [58, 59], which are in remarkable agreement, an experimentally-based estimate of B_ρ^{fit} from our RIGT measurements can be obtained and compared to the most accurate available calculation B_ρ^{calc} from [57] and to a recent estimate based on DCGT [63] results as reported in table 11.

5.4. Determination of thermodynamic temperature T by combining measurement results in helium and neon

In a publication by Schmidt *et al* [14] it was originally suggested that, for the sake of accurate pressure and temperature metrology, the determination of the effective compressibility of the apparatus might be avoided by combining resonance frequency determinations in two different atomic gases. If equation (1) is written for helium and neon for nominally equal (p, T) states, the terms containing κ_{eff} , which is gas-independent, and the zero pressure frequencies can be eliminated and the working equation becomes

$$\frac{n^{\text{Ne}}(p, T)}{n^{\text{He}}(p, T)} = \frac{\langle f_m^{\text{He}}(p, T) \rangle}{\langle f_m^{\text{Ne}}(p, T) \rangle}. \quad (24)$$

This method would be better implemented by a suitably designed ‘double’ experimental apparatus, comprising, for example, two resonators in good thermal contact but isolated

Table 11. Experimental fitted estimates of $(b_\varepsilon - B_\rho)$ in helium at five thermodynamic temperatures T . The superscripts ‘calc’ and ‘fit’ respectively refer to *ab initio* calculation [57, 60, 61] and to the linear extrapolation to zero pressure obtained in this work. The reported uncertainties for $(b_\varepsilon - B_\rho)^{\text{fit}}$ are those resulting from the fit procedure. Also listed are the $(b_\varepsilon - B_\rho)^{\text{DCGT}}$ estimates from recent DCGT experiments [63], where the reported uncertainties are standard uncertainties based on a complete uncertainty budget. The rightmost column lists the estimated values of B_ρ of Ne resulting from $(b_\varepsilon - B_\rho)^{\text{fit}}$ and calculated values of b_ε from [58, 59].

T (K)	$(b_\varepsilon - B_\rho)^{\text{calc}}$ (cm ³ mol ⁻¹) [57–59]	$(b_\varepsilon - B_\rho)^{\text{fit}}$ (cm ³ mol ⁻¹)	$(b_\varepsilon - B_\rho)^{\text{DCGT}}$ (cm ³ mol ⁻¹) [63]	B_ρ^{calc} (cm ³ mol ⁻¹) [57]	B_ρ^{fit} (cm ³ mol ⁻¹)
13.804	11.835 ± 0.018	11.824 ± 0.033	11.818 ± 0.046	−11.843 ± 0.002	−11.83 ± 0.03
24.555	−0.967 ± 0.010	−0.935 ± 0.021	−0.972 ± 0.028	0.9516 ± 0.0013	0.919 ± 0.021
54.355	−9.325 ± 0.005	−9.309 ± 0.017	−9.306 ± 0.018	9.2914 ± 0.0006	9.277 ± 0.017
83.802	−11.268 ± 0.003	−11.297 ± 0.030	−11.278 ± 0.029	11.2247 ± 0.0004	11.25 ± 0.03
161.401	−12.258 ± 0.002	−12.258 ± 0.078	−12.313 ± 0.137	12.1889 ± 0.0002	12.19 ± 0.08

Table 12. Uncertainty budget and $(T - T_{90})$ results for thermodynamic temperature determinations using a combination of helium and neon measurements using different methods of analysis. Weighted mean values of $(T - T_{90})$ and combined uncertainty of T are listed in boldface type.

T_{90} (K)	Method of analysis	Uncertainty source (mK)					$T - T_{90}$ (mK)	Combined uncertainty $u(T)$ (mK)
		$\kappa_{\text{eff}}(T)$	Modes’ dispersion	Frequency noise or extrapolation	Pressure	Theoretical value of A_ε, A_μ and B_ρ of He and Ne		
54.3584	Single state		0.65	0.20	0.64	1.59	−3.44	1.85
	Equation (20)	0.00	0.18	0.36	0.32	2.88	−3.43	2.92
	Equation (21)		0.57	0.17	0.31	1.62	−3.45	1.75
						Weighted mean	−3.44	1.17
83.8058	Single state		0.48	0.79	0.94	0.91	−5.37	1.60
	Equation (20)	0.00	0.30	0.45	0.46	1.48	−6.14	1.64
	Equation (21)		0.44	0.22	0.46	0.90	−5.30	1.12
						Weighted mean	−5.52	0.80
161.406	Single state		1.18	5.25	1.75	1.11	−10.03	5.76
	Equation (20)	0.00	0.85	1.42	0.87	1.38	−10.10	2.32
	Equation (21)		0.80	0.69	0.86	1.04	−10.11	1.72
						Weighted mean	−10.10	1.34

as far as gas mixing is concerned, and operated ensuring the two gas samples would be maintained at the same pressure and temperature. To test an imperfect realization of this concept, we combined the microwave frequency data separately acquired for He and Ne with the same apparatus by correcting them at the same reference values of pressure and temperature using the procedure illustrated in section 5.1 for each isotherm. When a close correspondence between pressure points was lacking in the neon or helium data series, like for example for the experimental isotherms at 54.4 K, spline interpolation was used to prepare the following data set:

$$\left(p_j, \frac{\langle f_m^{\text{He}}(p_j, T_i) \rangle}{\langle f_m^{\text{Ne}}(p_j, T_i) \rangle} \right), \quad (25)$$

which was then analyzed on the base of equations (8) and (9).

We remark that the two-gases frequency ratios in equation (24) differ significantly less from unity compared to those vacuum/pressure for the same gas. The consequent reduction of the sensitivity as a function of density, due to the reduced ‘effective’ polarizability, $(A_\varepsilon^{\text{Ne}} - A_\varepsilon^{\text{He}}) \sim 0.48 \times 10^{-6} \text{ m}^3 \text{ mol}^{-1}$ in equation (9), represents a fundamental drawback of this method. This problem could be partially overcome by combining the frequencies in He with those of

a more polarizable gas, i.e. argon, though this choice would further restrict the working range to temperatures above the triple point of argon $T \sim 85 \text{ K}$.

As for some other single-gas determinations, the precision of the analysis of the data in equation (24) is partly reduced by the limited working pressure range and by the uncertainty affecting the *ab initio* calculation of the density virial coefficients of neon. Thus, we used the optimized values of $(b_\varepsilon - B_\rho)^{\text{opt}}$ of Ne. In principle, this choice makes the two-gases determination of T not completely independent from the need of a compressibility estimate, since the preliminary optimization which leads to a revised estimate of B_ρ of Ne procedure requires an estimate of κ_{eff} . Also, we remark that an implicit assumption of equation (24) is that the vacuum frequencies would remain unchanged over the time lapse between measuring in helium and neon. We found that this was not the case for our combined He and Ne isotherms, with the determination of T being sensibly affected by the slight changes of the vacuum frequencies recorded before measuring in He and, at a distance of months and after multiple pressure and temperature cycles, before measuring in Ne. Following this evidence, we accounted for isotherm- and gas-specific vacuum frequencies by the ratios:

$$r_m^{\text{He,Ne}}(p_j, T_i) = \frac{\langle f_m^{\text{He,Ne}}(p_j, T_i) \rangle}{\langle f_m^{\text{He,Ne}}(0, T_i) \rangle}, \quad (26)$$

to construct a new data set:

$$\left(p_j, \frac{r_m^{\text{He}}(p_j, T_i)}{r_m^{\text{Ne}}(p_j, T_i)} \right) \quad (27)$$

which was analyzed using the same three methods, direct single state and the linear extrapolation to zero pressure with or without a constrained intercept, previously used to analyze He data (see section 5.2). The corresponding results and uncertainty budgets are reported in table 12. These two-gases results are evidently affected by large combined uncertainties in comparison to single-gas evaluations, mainly as a consequence of the reduced precision discussed above, otherwise the corresponding $(T - T_{90})$ estimates are consistent with the other determinations presented in this work.

6. Concluding remarks and prospects of RIGT improvement

The thermodynamic temperature determinations presented and discussed in this work, in consideration of their remarkable agreement with previous results and interpolations, confirm the validity of RIGT as an accurate primary thermometry method. At the same time, some inherent difficulties of the method were also confirmed, and a demonstration of the full potential of RIGT as a suitable method for the future direct dissemination of the kelvin awaits further developments.

Particularly, a major pending issue is the accurate determination of the effective compressibility of the apparatus which is required by the method. In this work, this requirement was addressed by additional microwave measurements at the reference temperature of 273.16 K and by a RUS determination of the Grüneisen parameters needed to extrapolate the microwave result over a wide range of temperatures. Such considerable experimental effort limits the practical application of the method as κ_{eff} , which is a property of the apparatus rather than of the comprising material, may be subject to variations which are hard to predict or detect unless the effort of its determination is periodically repeated. A promising strategy to overcome this problem is based on the use of two different thermometric gases at the same temperature. In this work we explored this possibility, as discussed in section 5.4, but we were only partially successful because of the limited pressure range of our apparatus. A wider pressure is also a necessary requisite to increase the accuracy of the method at temperatures near ambient. Obviously, use of two different thermometric gases doubles the time needed for the determination of T and is only possible at temperatures above about 40 K where Ne exists in the vapour phase over a suitable pressure range. At lower temperatures, the single pressure version of the method dubbed SPRIGT and developed at TIPC-CAS represents a promising alternative though this relative method requires, as a reference, at least an additional primary thermometry result [6].

With regard to the best implementation of RIGT, among several possible methods of analysis of microwave data which

have been considered and compared in this work, it appears that the so-called single state method would be preferable for practical work, as it requires a fraction of the experimental work needed to collect data at several pressures along an isotherm. However, the analysis of the latter more complete records by extrapolation to zero pressure demonstrated superior accuracy.

Finally, it is worth noting the fundamental role of *ab initio* calculations of the thermodynamic and electromagnetic properties of monatomic gases. The present results exploit the outstanding accuracy achieved by these calculations for helium. Future developments of RIGT await the time when calculations of comparable accuracy for neon and argon will be available. Given the highly remarkable progress recently made in the calculation of some electrical properties of neon [58, 59, 62] the current perspectives do indeed look promising for the future of gas-based primary thermometry.

Acknowledgments

This work was carried out within the projects ‘Implementing the new Kelvin 2—InK2’ and ‘Realising the New Kelvin—Real K’. These projects (15SIB02 InK 2) and (18SIB02 Real K) have received funding from the EMPIR programme which is co-financed by the Participating States and from the European Union’s Horizon 2020 research and innovation programme. We are grateful to the National Institute of Standards and Technology (NIST) for the loan of the pressure balance used in this work. We are extremely thankful to Patrick Rourke for his careful reading of a preliminary draft of this manuscript and the many useful suggestions he provided to improve it.

Supplementary data

This article is combined with a supplementary section which comprises:

Original microwave data for 8 isotherms with two thermometric gases (He and Ne) with separate records for each pressure investigated along each isotherm; these datasets would allow the interested reader to reproduce and check all the analysis which leads to the $(T - T_{90})$ determinations obtained in this work;





Detailed uncertainty budgets for the calibration of cSPRTs at the ITS-90 fixed points as realized and maintained at INRiM in the range between the triple point of equilibrium hydrogen ($T_{90} = 13.8033$ K) and the triple point of water ($T_{90} = 273.16$ K).

All these data are listed in a single spreadsheet file: METabe249supp2.xls. Additional information regarding the organization of the data is available in a separate text file: METabe249supp1.pdf.

ORCID iDs

D Madonna Ripa  <https://orcid.org/0000-0002-8760-8574>

D Imbraguglio  <https://orcid.org/0000-0002-1289-772x>

C Gaiser  <https://orcid.org/0000-0003-1745-7368>
 P P M Steur  <https://orcid.org/0000-0001-5161-8554>
 G Lopardo  <https://orcid.org/0000-0002-5250-0459>
 R M Gavioso  <https://orcid.org/0000-0002-1631-5133>

References

- [1] Fischer J *et al* 2011 Present estimates of the differences between thermodynamic temperatures and the ITS-90 *Int. J. Thermophys.* **32** 12–25
- [2] Rourke P M C, Gaiser C, Gao B, Madonna Ripa D, Moldover M R, Pitre L and Underwood R J 2019 Refractive-index gas thermometry *Metrologia* **56** 032001
- [3] Gaiser C, Fellmuth B and Haft N 2020 Thermodynamic-temperature data from 30 K to 200 K *Metrologia* **57** 055003
- [4] Rourke P M C 2017 NRC microwave refractive index gas thermometry implementation between 24.5 K and 84 K *Int. J. Thermophys.* **38** 107
- [5] Rourke P M C 2020 Thermodynamic temperature of the triple point of xenon measured by refractive index gas thermometry *Metrologia* **57** 024001
- [6] Gao B *et al* 2020 Measurement of thermodynamic temperature between 5 K and 24.5 K with single-pressure refractive-index gas thermometry *Metrologia* **57** 065006
- [7] Underwood R, de Podesta M, Sutton G, Stanger L, Rusby R, Harris P, Morantz P and Machin G 2016 Estimates of the difference between thermodynamic temperature and the International Temperature Scale of 1990 in the range 118 K to 303 K *Phil. Trans. R. Soc. A* **374** 20150048
- [8] Gaiser C, Zandt T and Fellmuth B 2015 Dielectric-constant gas thermometry *Metrologia* **52** S217
- [9] Gaiser C, Fellmuth B and Haft N 2017 Primary thermometry from 2.5 K to 140 K applying dielectric-constant gas thermometry *Metrologia* **54** 141–7
- [10] Kytin V G, Kytin G A, Ghavalyan M Y, Potapov B G, Aslanyan E G and Schipunov A N 2020 Deviation of temperature determined by ITS-90 temperature scale from thermodynamic temperature measured by acoustic gas thermometry at 79.0000 K and at 83.8058 K *Int. J. Thermophys.* **41** 88
- [11] May E F, Pitre L, Mehl J B, Moldover M R and Schmidt J W 2004 Quasi-spherical cavity resonators for metrology based on the relative dielectric permittivity of gases *Rev. Sci. Instrum.* **75** 3307–17
- [12] Pitre L, Moldover M R and Tew W L 2006 Acoustic thermometry: new results from 273 K to 77 K and progress towards 4 K *Metrologia* **43** 142–62
- [13] Moldover M R, Gavioso R M, Mehl J B, Pitre L, de Podesta M and Zhang J T 2014 Acoustic gas thermometry *Metrologia* **51** R1–R19
- [14] Schmidt J W, Gavioso R M, May E F and Moldover M R 2007 Polarizability of helium and gas metrology *Phys. Rev. Lett.* **98** 254504
- [15] Gao B *et al* 2018 Realization of an ultra-high precision temperature control in a cryogen-free cryostat *Rev. Sci. Instrum.* **89** 104901
- [16] Astrov D N, Beliansky L B, Dedikov Y A, Polunin S P and Zakharov A A 1989 Precision gas thermometry between 2.5 K and 308 K *Metrologia* **26** 151–66
- [17] Pan C, Chen H, Han D, Zhang H, Plimmer M, Imbraguglio D, Luo E, Gao B and Pitre L 2020 Numerical and experimental study of the hydrostatic pressure correction in gas thermometry: a case in the SPRIGT *Int. J. Thermophys.* **41** 108
- [18] D'Agostino G, Desogus S, Germak A, Origlia C, Quagliotti D, Celli G and Francis O 2006 Measurements of the acceleration due to gravity at the gravity laboratory of the National Institute of Metrological Research Turin *Technical Report* (Italy, INRiM) 33
- [19] Gavioso R M, Madonna Ripa D, Steur P P M, Gaiser C, Truong D, Guianvarc'h C, Tarizzo P, Stuart F M and Dematteis R 2015 A determination of the molar gas constant *R* by acoustic thermometry in helium *Metrologia* **52** S274–304
- [20] Gavioso R M, Madonna Ripa D, Steur P P M, Dematteis R and Imbraguglio D 2019 Determination of the thermodynamic temperature between 236 K and 430 K from speed of sound measurements in helium *Metrologia* **56** 045006
- [21] Yang I, Underwood R and de Podesta M 2018 Investigating the adequacy of a low-cost vector network analyser for microwave measurements in quasispherical resonators *Meas. Sci. Technol.* **29** 075013
- [22] Simon N J, Drexler E S and Reed R P 1992 Properties of copper and copper alloys at cryogenic temperatures *NIST Monograph 177* (Washington, DC: US Government Printing Office)
- [23] Rourke P M C and Hill K D 2015 Progress toward development of low-temperature microwave refractive index gas thermometry at NRC *Int. J. Thermophys.* **36** 205–28
- [24] Inagaki S, Ezura E, Liu J-F and Nakanishi H 1997 Thermal expansion and microwave surface reactivity of copper from the normal to anomalous skin effect region *J. Appl. Phys.* **82** 5401–10
- [25] Underwood R J, Mehl J B, Pitre L, Edwards G, Sutton G and de Podesta M 2010 Waveguide effects on quasispherical microwave cavity resonators *Meas. Sci. Technol.* **21** 075103
- [26] Mehl J B 2009 Second-order electromagnetic eigenfrequencies of a triaxial ellipsoid *Metrologia* **46** 554–9
- [27] Preston-Thomas H 1990 The international temperature scale of 1990 (ITS-90) *Metrologia* **27** 3–10
- [28] Imbraguglio D, Steur P P M and Sparasci F 2020 Comparison of ITS-90 realizations from 13 K to 273 K between LNE-CNAM and INRiM *Measurement* **166** 108225
- [29] Fellmuth B, Mendez-Lango E, Nakano T and Sparasci F 2017 Guide to the realization of the ITS-90, cryogenic fixed points <https://bipm.org/utis/common/pdf/ITS-90/Guide-ITS-90-Cryogenic-Fixed-Points-2017.pdf>
- [30] Pearce J V, Steur P P M, Joung W, Sparasci F, Strouse G, Tamba J and Kalemci M 2018 Guide to the realization of the ITS-90, metal fixed points for contact thermometry https://bipm.org/utis/common/pdf/ITS-90/Guide-ITS-90_2_4_MetalFixedPoints_2018.pdf
- [31] Marcarino P, Steur P P M and Dematteis R 2003 Realization at IMGC of the ITS-90 fixed points from the argon triple point Upwards *AIP Conf. Proc.* **684** 65–70
- [32] Consultative Committee for Thermometry of the BIPM 2019 Mise en pratique for the definition of the kelvin in the SI, Appendix 2 of the SI Brochure 9th edition <https://www.bipm.org/utis/en/pdf/si-mep/SI-App2-kelvin.pdf>
- [33] Pokhodun A I, Fellmuth B, Pearce J V, Rusby R L, Steur P P M, Tamura O, Tew W L and White D R 2016 Guide to the realization of the ITS-90, platinum resistance thermometry, APPENDIX 2: typical resistance ratios and sensitivity factors for SPRTs in the ITS-90, as well as the propagation of uncertainty at the triple point of water <https://bipm.org/utis/common/pdf/ITS-90/Guide-ITS-90-Platinum-Resistance-Thermometry-Appendix2.pdf>
- [34] Steur P P M, Rourke P M C and Giraudi D 2019 Comparison of xenon triple point realizations *Metrologia* **56** 015008
- [35] Hill K D and Steele A G 2003 The non-uniqueness of the ITS-90: 13.8033 K to 273.16 K *Temperature, Its Measurement and Control in Science and Industry* vol 7 (New York: AIP) pp 53–8
- [36] White D R *et al* 2007 Uncertainties in the realization of the SPRT sub-ranges of the ITS-90 *Int. J. Thermophys.* **28** 1868–81

- [37] Gaiser C and Fellmuth B 2016 Method for extrapolating the compressibility data of solids from room to lower temperatures *Phys. Status Solidi* **253** 1549–56
- [38] Grüneisen E 1912 Theorie des festen zustandes einatomiger elemente *Ann. Phys.* **344** 257–306
- [39] Maynard J D 1992 The use of piezoelectric film and ultrasound resonance to determine the complete elastic tensor in one measurement *J. Acoust. Soc. Am.* **91** 1754–62
- [40] Migliori A, Sarrao J L, Visscher W M, Bell T M, Lei M, Fisk Z and Leisure R G 1993 Resonant ultrasound spectroscopic techniques for measurement of the elastic moduli of solids *Physica** **183** 1–24
- [41] Zandt T, Gaiser C, Fellmuth B, Haft N, Thiele-Krivoi B and Kuhn A 2013 Use of the finite-element method for a dielectric-constant gas-thermometry experiment *AIP Conf. Proc.* **1552** 130–5
- [42] Visscher W M, Migliori A, Bell T M and Reinert R A 1991 *J. Acoust. Soc. Am.* **90** 2154–62
- [43] Ledbetter H M 1980 Sound velocities and elastic-constant averaging for polycrystalline copper *J. Phys. D: Appl. Phys.* **13** 1879
- [44] Ledbetter H M 1981 Elastic constants of polycrystalline copper at low temperatures. Relationship to single-crystal elastic constants *Phys. Status Solidi** **66** 477
- [45] Puchalski M, Piszczatowski K, Komasa J, Jeziorski B and Szalewicz K 2016 Theoretical determination of the polarizability dispersion and the refractive index of helium *Phys. Rev. A* **93** 032515
- [46] Puchalski M, Szalewicz K, Lesiuk M and Jeziorski B 2020 QED calculation of the dipole polarizability of helium atom *Phys. Rev. A* **101** 022505
- [47] Gaiser C and Fellmuth B 2018 Polarizability of helium, neon, and argon: new perspectives for gas metrology *Phys. Rev. Lett.* **120** 123203
- [48] Bruch L W and Weinhold F 2002 Nuclear motion and Breit–Pauli corrections to the diamagnetism of atomic helium *J. Chem. Phys.* **117** 3243–7
- [49] Bruch L W and Weinhold F 2003 Nuclear motion and Breit–Pauli corrections to the diamagnetism of atomic helium *J. Chem. Phys.* **119** 638 (erratum)
- [50] Barter C, Meisenheimer R G and Stevenson D P 1960 Diamagnetic susceptibilities of simple hydrocarbons and volatile hydrides *J. Phys. Chem.* **64** 1312–6
- [51] Cencek W, Przybytek M, Komasa J, Mehl J B, Jeziorski B and Szalewicz K 2012 Effects of adiabatic, relativistic, and quantum electrodynamics interactions on the pair potential and thermophysical properties of helium *J. Chem. Phys.* **136** 224303
- [52] Garberoglio G, Moldover M R and Harvey A H 2011 Improved first-principles calculation of the third virial coefficient of helium *J. Res. Natl. Inst. Stand. Technol.* **116** 729–42
- [53] Shaul K R S, Schultz A J and Kofke D A 2012 Path-integral Mayer-sampling calculations of the quantum Boltzmann contribution to virial coefficients of helium-4 *J. Chem. Phys.* **137** 184101
- [54] Rizzo A, Hättig C, Fernández B and Koch H 2002 The effect of intermolecular interactions on the electric properties of helium and argon. III. Quantum statistical calculations of the dielectric second virial coefficients *J. Chem. Phys.* **117** 2609–18
- [55] Cencek W, Komasa J and Szalewicz K 2011 Collision-induced dipole polarizability of helium dimer from explicitly correlated calculations *J. Chem. Phys.* **135** 014301
- [56] Heller D F and Gelbart W M 1974 Short range electronic distortion and the density dependent dielectric function of simple gases *Chem. Phys. Lett.* **27** 359–64
- [57] Czachorowski P, Przybytek M, Lesiuk M, Puchalski M and Jeziorski B 2020 Second virial coefficients for ^4He and ^3He from an accurate relativistic interaction potential *Phys. Rev. A* **102** 042810
- [58] Garberoglio G and Harvey A H 2020 Path-integral calculation of the second dielectric and refractivity virial coefficients of helium, neon, and argon *J. Res. Natl. Inst. Stand. Technol.* **125** 125022
- [59] Song B and Luo Q-Y 2020 Accurate second dielectric virial coefficient of helium, neon, and argon from *ab initio* potentials and polarizabilities *Metrologia* **57** 025007
- [60] Bich E, Hellmann R and Vogel E 2008 *Ab initio* potential energy curve for the neon atom pair and thermophysical properties for the dilute neon gas. II. Thermophysical properties for low density neon *Mol. Phys.* **106** 1107–22
- [61] Hättig C, Cacheiro J, Fernández B and Rizzo A 2003 *Ab initio* calculation of the refractivity and hyperpolarizability second virial coefficients of neon gas *Mol. Phys.* **101** 1983–95
- [62] Lesiuk M, Przybytek M and Jeziorski B 2020 Theoretical determination of polarizability and magnetic susceptibility of neon *Phys. Rev. A* **102** 052816
- [63] Gaiser C and Fellmuth B 2020 Highly-accurate second-virial-coefficient values for helium from 3.7 K to 273 K determined by dielectric-constant gas thermometry *Metrologia* **58** 015013